

Pulsational Analysis of the Cores of Massive Stars and its Relevance to Pulsar Kicks

Jeremiah W. Murphy^{1,2}

Adam Burrows¹

and

Alexander Heger^{3,4}

ABSTRACT

The mechanism responsible for the natal kicks of neutron stars continues to be a challenging problem. Indeed, many mechanisms have been suggested, and one hydrodynamic mechanism may require large initial asymmetries in the cores of supernova progenitor stars. Goldreich, Lai, & Sahriling (1997) suggested that unstable g-modes trapped in the iron (Fe) core by the convective burning layers and excited by the ϵ -mechanism may provide the requisite asymmetries. We perform a modal analysis of the last minutes before collapse of published core structures and derive eigenfrequencies and eigenfunctions, including the nonadiabatic effects of growth by nuclear burning and decay by both neutrino and acoustic losses. In general, we find two types of g-modes: inner-core g-modes, which are stabilized by neutrino losses and outer-core g-modes which are trapped near the burning shells and can be unstable. Without exception, we find at least one unstable g-mode for each progenitor in the entire mass range we consider, 11 M_{\odot} to 40 M_{\odot} . More importantly, we find that the timescales for growth and decay are an order of magnitude or more longer than the time until the commencement of core collapse. We conclude that the ϵ -mechanism may not have enough time to significantly amplify core g-modes prior to collapse.

Subject headings:

1. Introduction

Observations indicate that many pulsars have high proper motions (Lyne & Lorimer 1994; Lorimer, Bailes, & Harrison 1997; Hansen & Phinney 1997; Cordes & Chernoff 1998) and that many neutron star systems require kicks at birth. For example, pulsar bow shock morphologies (Cordes, Romani, & Lundgren 1993), misaligned spins of binary pulsars (Cordes, Wasserman, & Blaskiewicz 1990; Kramer 1998; Wex, Kalogera, & Kramer 2000; Kaspi et al. 1996; Lai, Bildsten, & Kaspi 1995; Lai 1996; Kumar & Quataert 1997), the statistics of low-mass X-ray binaries (LMXBs) (Kalogera 1997; Kalogera & Webbink 1998), the

¹Steward Observatory, The University of Arizona, Tucson, AZ 85721; jmurphy@as.arizona.edu, aburrows@as.arizona.edu

²JINA Fellow.

³Theoretical Astrophysics Group, T-6, MS B227, Los Alamos National Laboratory, Los Alamos, NM 87544, U.S.A.; alex@t6.lanl.gov

⁴Enrico Fermi Institute, The University of Chicago, 5640 S Ellis Ave., Chicago, IL, 60637, U.S.A.

high orbital eccentricities of some Be star systems (Verbunt & van den Heuvel 1995), and scenarios for double neutron star systems (Dewey & Cordes 1987; Fryer & Kalogera 1997; Fryer, Burrows, & Benz 1998; Dewi & van den Heuvel 2004; Willems & Kalogera 2004) all indicate that neutron stars experience significant natal kicks. Furthermore, Arzoumanian, Chernoff, & Cordes (2002) find a bimodal distribution of birth kick speeds with peaks at $\sim 100 \text{ km s}^{-1}$ and $\sim 700 \text{ km s}^{-1}$ and dispersions of 90 and 500 km s^{-1} . They suggest that roughly 50% of the pulsars in the solar neighborhood escape the Galaxy and that $\sim 15\%$ have kick speeds greater than 1000 km s^{-1} . The observations indicate that kicks seem to be hallmarks of neutron star formation.

What is the mechanism producing the observed and inferred kicks? To give a $1.4 M_{\odot}$ neutron star a speed of 1000 km s^{-1} , the mechanism must be able to impart $\sim 10^{49}$ erg of kinetic energy, which is just 1% of the canonical SN mechanical energy ($\sim 10^{51}$ erg) or 0.01% of the collapse energy ($\sim 10^{53}$ erg). Additionally, any explanation must address the distribution of speeds. If the distribution is bimodal, then it is possible that more than one mechanism is responsible for the kicks. Lai (2000b) has summarized the possible magnetic, neutrino (ν), and hydrodynamic kick mechanisms, but in general many of the scenarios have trouble producing kicks larger than $\sim 200 \text{ km s}^{-1}$.

Of the many mechanisms propounded, hydrodynamic mechanisms are the most compelling. For example, neutrino-driven convection, which is inherently a nonspherical phenomenon, excites large-scale convective motions that stochastically jostle the protoneutron star (Burrows, Hayes, & Fryxell 1995; Janka & Müller 1994). However, multi-dimensional calculations indicate that any kick imparted as a result of the convective jostling (“Brownian motion”) has an average magnitude of $\sim 200 \text{ km s}^{-1}$ (Burrows et al. 1995; Janka & Müller 1994; Scheck et al. 2004) and cannot explain the highest velocities nor the second peak in a possible bimodal distribution.

These analyses suggest the need for additional asymmetries before the onset of collapse. Burrows & Hayes (1996) state that global asymmetries in the progenitor may be prerequisites for large kicks. In a 2-D hydrodynamic simulation and with modest asymmetries, Burrows & Hayes (1996) are able to produce a recoil speed of $\sim 550 \text{ km s}^{-1}$. However, these calculations are crude and the results, while suggestive, are not conclusive. Goldreich et al. (1997) have proposed that these asymmetries may be excited by the ϵ -mechanism in which g-mode oscillations in the core are pumped by nuclear reactions.

As a prelude to more definitive multi-dimensional radiation hydrodynamic investigations of neutron star kicks in the supernova context, one would like to determine whether global asymmetries prior to core collapse in fact occur. Hence, a thorough analysis of the progenitor oscillations and their growth rates is necessary. In this paper, we explore the viability of the g-mode oscillation origin for putative pre-collapse anisotropies by performing such an eigenmode analysis.

2. Linear Perturbation Equations

To set the stage for our eigenmode analysis of the cores of nonrotating massive stars, we first describe linear stellar pulsation theory in the general case. In linear perturbation theory, a star is assumed to be in hydrostatic equilibrium, around which perturbations are small, making second-order or higher terms in the perturbation equations negligibly small. Therefore, if $f_0(\vec{r})$ is a quantity satisfying the hydrostatic equations, then $f(\vec{r}, t) \rightarrow f_0(r) + f'(\vec{r}, t)$, where 0 denotes the background solution and $'$ denotes the Eulerian perturbation. We assume that the perturbation is of the form $f'(\vec{r}, t) = f'(r)Y_{\ell m}(\theta, \phi)e^{i\omega t}$, where $Y_{\ell m}(\theta, \phi)$ is a spherical harmonic in that ℓ and m are the polar and azimuthal indices, respectively, and ω is the oscillation

frequency. Under these assumptions and an assumption of adiabatic perturbations, if P , ρ , ϕ , c_s are the pressure, density, gravitational potential, and sound speed, respectively, the adiabatic linear perturbation equations¹ are

$$\frac{1}{r^2} \frac{d}{dr} (r^2 \xi_r) - \frac{g}{c_s^2} \xi_r + \left(1 - \frac{L_\ell^2}{\omega^2}\right) \frac{P'}{\rho c_s^2} = \frac{l(l+1)}{\omega^2 r^2} \phi', \quad (1)$$

$$\frac{1}{\rho} \frac{dp'}{dr} + \frac{g}{\rho c_s^2} P' + (N^2 - \omega^2) \xi_r = -\frac{d\phi'}{dr}, \quad (2)$$

and

$$\frac{1}{r^2} \frac{d}{dr} \left(r^2 \frac{d\phi'}{dr} \right) - \frac{l(l+1)}{r^2} \phi' = 4\pi G \rho \left(\frac{P'}{\rho c_s^2} + \frac{N^2}{g} \xi_r \right). \quad (3)$$

ξ_r and ξ_h are the radial and horizontal components of the Lagrangian displacement vector, $\vec{\xi} = \vec{r} - \vec{r}_0$, and are defined by

$$\vec{\xi} = \left(\xi_r, \xi_h \frac{\partial}{\partial \theta}, \xi_h \frac{\partial}{\sin \theta \partial \phi} \right) Y_{lm}(\theta, \phi) e^{i\omega t} \quad (4)$$

and

$$\xi_h = \frac{1}{\omega^2 r} \left(\frac{P'}{\rho} + \phi' \right). \quad (5)$$

N and L_ℓ are the Brunt-Väisälä and Lamb frequencies, respectively, which are given by

$$N^2 = g \left(\frac{1}{\Gamma_1} \frac{d \ln P}{dr} - \frac{d \ln \rho}{dr} \right) \quad (6)$$

and

$$L_\ell^2 = \frac{\ell(\ell+1)c_s^2}{r^2}, \quad (7)$$

where $g = GM_r/r^2$, G is the gravitational constant, and M_r is the mass interior to r .

Equations (1), (2), and (3) represent a fourth-order boundary value problem. Near $r \sim 0$, simplifications and regularity in the variables ϕ' , ξ_r , and $(P'/\rho + \phi')$ dictate that the inner boundary conditions are

$$\frac{d\phi'}{dr} - \frac{\ell\phi'}{r} = 0 \quad (8)$$

and

$$\xi_r - \ell\xi_h = 0. \quad (9)$$

At the surface of the calculational domain, $r = R$ or $M_r = M$, one outer boundary condition, from the regularity of ϕ' , is

$$\frac{d\phi'}{dr} + \frac{(l+1)}{r} \phi' = 0. \quad (10)$$

A second outer boundary condition allows for the possibility that the atmosphere is either evanescent to both p- and g-waves or progressive to outgoing p-waves (Lai 2000b), depending upon the mode frequency:

$$\left(\frac{\lambda_- - (V/\Gamma_1 - 3)}{b_1} \right) \frac{\xi_r}{r} - \frac{\omega^2}{g} \xi_h - \left(\frac{\alpha_1(\lambda_- - (V/\Gamma_1 - 3))}{b_1} - \alpha_2 \right) \frac{\phi'}{gr} = 0, \quad (11)$$

where

$$\lambda_- = \frac{1}{2} \left(\frac{V}{\Gamma_1} + \frac{rN^2}{g} - 2 - \gamma^{1/2} \right), \quad (12)$$

¹For a complete derivation of the adiabatic linear perturbation equations see Unno et al. (1989).

$$\gamma = \left(\frac{rN^2}{g} - \frac{V}{\Gamma_1} + 4 \right)^2 + 4 \left(\ell(\ell+1) \frac{GM}{\omega^2 R^3} - \frac{V}{\Gamma_1} \right) \left(\frac{\omega^2 R^3}{GM} - \frac{rN^2}{g} \right), \quad (13)$$

$$b_1 = \frac{\ell(\ell+1)\omega^2 R^3}{GM} - \frac{V}{\Gamma_1}, \quad (14)$$

$$b_2 = \frac{\omega^2 R^3}{GM} - \frac{rN^2}{g}, \quad (15)$$

$$\alpha_1 = \frac{b_1(rN^2/g) - ((1+rN^2/g) + \ell)V/\Gamma_1}{(V/\Gamma_1 - 3 + \ell)(1+rN^2/g + \ell) - b_1 b_2}, \quad (16)$$

and

$$\alpha_2 = \frac{b_2 V/\Gamma_1 - (V/\Gamma_1 - 3 + \ell)rN^2/g}{(V/\Gamma_1 - 3 + \ell)(1+rN^2/g + \ell) - b_1 b_2}. \quad (17)$$

If the mode frequency is such that this boundary condition represents leakage of mode energy by progressive p-waves then the eigensolutions are complex, with the imaginary part of ω , ω_I , being related to the rate of leakage.

The solutions to the boundary and eigenvalue problem as defined by eqs. (1)-(3) with the boundary conditions, eqs. (8)-(11), are the eigenmodes of the perturbed star. The eigenvalue, ω^2 , and eigensolution depend on the stellar structure and spherical harmonic index, ℓ , but without rotation are degenerate for different values of m . We have found solutions to this boundary value problem using a shooting technique, in which we search for all modes within a region of the complex plane of ω^2 . This is accomplished with a 2-D Newton-Raphson technique, where convergence to one part in 10^6 , or better, in the eigenvalue is required. We compare our eigensolutions and eigenfrequencies for the standard Solar model (Christensen-Dalsgaard et al. 1996) with the eigenmodes determined by a publicly accessible Fortran code² designed to solve the adiabatic linear perturbation equations. The agreement between the two is better than 0.1%.

2.1. Work Integral

In general, non-adiabatic effects such as nuclear burning and neutrino emission are included in the perturbation equations. However, if these terms are small, the contributions to the imaginary part of ω , ω_I , which is directly related to the rate of growth or decay of the mode, can be obtained from the time-averaged work integral, W_j (Unno et al. 1989). For a quasi-adiabatic oscillation,

$$W_j = \frac{\pi}{\omega} \int_0^M \epsilon_j \left(\epsilon_{jT} + \frac{\epsilon_{j\rho}}{\Gamma_3 - 1} \right) \left| \frac{\delta T}{T} Y_{lm}(\theta, \phi) \right|^2 dM_r, \quad (18)$$

where ϵ_j (erg g⁻¹ s⁻¹) is the deposition or loss of energy by either nuclear heating if $j = nuc$ or neutrino losses if $j = \nu$. Furthermore, $\epsilon_{jT} = (\partial \ln \epsilon_j / \partial \ln T)_\rho$, $\epsilon_{j\rho} = (\partial \ln \epsilon_j / \partial \ln \rho)_T$, and $\Gamma_3 - 1 \equiv (\partial \ln T / \partial \rho)_S$, where S is the entropy. The radial distribution of the Lagrangian perturbation in temperature is given by

$$\frac{\delta T}{T} = V \nabla_{ad} \left(\frac{\omega^2}{g} \xi_h - \frac{\phi'}{gr} - \frac{\xi_r}{r} \right), \quad (19)$$

where $\nabla_{ad} = (\partial \ln T / \partial \ln \rho)_s$ and $V = gr\rho/P$.

²provided by J. Christensen-Dalsgaard <http://astro.phys.au.dk/~jcd/adipack.n/>

When ω is complex, as is the case when the mode gains or loses energy, the time dependence of the modes may be written as

$$\vec{\xi} \propto e^{i\omega_R t} e^{t/\tau}, \quad (20)$$

where ω_R is the real part of ω , and τ is the timescale for growth (+) or decay (-) and is a composite effect determined by the equation

$$\frac{1}{\tau} = \frac{1}{\tau_{nuc}} + \frac{1}{\tau_\nu} + \frac{1}{\tau_{leak}}. \quad (21)$$

τ_{nuc} , τ_ν , and τ_{leak} include the effects of nuclear gains, neutrino losses, and acoustic losses, respectively. The nuclear and neutrino timescales are related to their respective work integrals by

$$\tau_j = \frac{4\pi E_W}{\omega_R W_j}, \quad (22)$$

where E_W is the energy in the mode:

$$E_W = \frac{\omega_R^2}{2} \int_0^M |\vec{\xi}|^2 dM_r, \quad (23)$$

and τ_{leak} is directly determined by the imaginary part of ω , $Im(\omega) = -1/\tau_{leak}$. This quantity is the solution to the adiabatic linear perturbation equations when eq. (11) is the fourth boundary condition. The modes are stable or unstable for $\tau < 0$ or $\tau > 0$, respectively.

3. Massive Star Structures

To investigate the character of the eigenmodes as a function of progenitor mass and time, t , prior to the onset of collapse, we consider the cores of nonrotating, massive stars with masses of 11 M_\odot , 13 M_\odot , 15 M_\odot , 25 M_\odot , 30 M_\odot , 35 M_\odot and 40 M_\odot (Rauscher et al. 2002; Woosley, Heger, & Weaver 2002) and at $t = 3600, 600, 60, 30, 25, 20, 15, 10, 5, 2, 1$, and 0 (start of collapse) seconds before the onset of collapse. The commencement of collapse is defined at the time when the peak infall velocity exceeds 900 km s⁻¹. This is about 200 to 250 ms before core bounce. The structure of each stellar model uniquely determines its eigenmodes. Thus, an identification of important trends in the models is helpful in characterizing these modes. In the top panel of Fig. 1 we see that more massive models have higher entropy, translating into lower central densities and more extended density (ρ) versus interior mass, M_r , profiles. Consequently, prominent boundaries which are associated with discontinuities in entropy and Y_e and which affect the character of the modes are also located at larger radii for higher-mass progenitors. These discontinuities are the boundary between the fossil Fe core (the residue of core Si burning) and the most recent Fe ashes from shell Si burning (circles on Fig. 1), the edge of the Fe core (includes the fossil Fe core and recent Fe ashes) and the Si burning shell (stars on Fig. 1), and the interface between the Si burning and O burning shells (triangles on Fig. 1). The general structural profiles and these distinct boundaries (Table 1) together determine the eigenfunctions and eigenfrequencies.

The role of structure in affecting the general character of the solutions can be understood using the local dispersion relation for plane waves of the form $e^{i(\vec{k} \cdot \vec{r} \pm \omega t)}$:

$$k_r^2 = \frac{(N^2 - \omega^2)(L_\ell^2 - \omega^2)}{c_s^2 \omega^2}, \quad (24)$$

where k_r is the radial component of the wave vector (Unno et al. 1989). This relation implies that for $N^2 < \omega^2 < L_\ell^2$, all waves are evanescent, for $N^2 < L_\ell^2 < \omega^2$, they are p-waves, and for $\omega^2 < N^2 < L_\ell^2$,

they are g-waves (Unno et al. 1989). A propagation diagram, which plots N^2 and L_ℓ^2 versus M_r or r , shows where in the star each type of wave is allowed to propagate. The propagation diagrams for the 13 M_\odot (top panel) and 30 M_\odot (bottom panel) models and their corresponding density and Y_e profiles, are presented in Fig. 2. The positions of the prominent discontinuities are marked as in Fig. 1. Rather than plotting N^2 and L_ℓ^2 , the equivalent period has been presented for each. These periods are $P_{Brunt} = 2\pi/\sqrt{|N^2|}$ and $P_{Lamb} = 2\pi/\sqrt{L_\ell^2}$. An important feature illustrated in Fig. 2 is that N^2 rises and then falls, creating a resonant cavity for g-modes. The fall is partly due to the density and pressure structures, but on the outside it dramatically plummets due to convection in the O-burning shell, thereby confining g-waves within the core. For higher frequencies (lower periods), p-waves are allowed. However, they are free to propagate throughout the entire star. Since the sound-crossing time in the outer stellar mantle is extremely long and dissipative processes exist, the establishment of standing p-modes is prevented. Hence, for all models and times, g-modes are trapped in the core, encompassing the Fe core and frequently the Si burning shell.

Other salient features evident in Fig. 2 are the spikes in P_{Brunt} , or equivalently, N^2 . These spikes are the result of S , Y_e , and ρ discontinuities at the boundaries indicated in Table 1. As impedance mismatches these spikes effectively reflect g-waves. Therefore, even though most g-modes have their greatest amplitude near the center of the core, the reflecting boundaries imply that there might be sub-regions within the overall resonating cavity in which modes may be trapped.

By prodigious neutrino emission, the cores of massive stars continue to change their structures prior to the onset of core collapse (Woosley et al. 2002). Figure 3 illustrates the changes of the propagation diagram for the 13 M_\odot model during the last ten minutes of evolution. As the inner regions quickly evolve and contract, the Brunt-Väisälä frequency increases with time, gradually increasing the modal frequencies. In contrast, the model corresponding to $t = 0$ s (onset of collapse) exhibits a dramatic truncation in the size of the resonating cavity, in that N^2 drops to negative values as the convective region grows due to implosive burning. However, collapse happens on a dynamical timescale, and will take 200 to 250 ms. Given that the convective turnover times and the periods of oscillation are longer than this, the assumption of steady-state mixing-length convection is probably violated. Although for completeness, results for the $t = 0$ s models are presented here, the quantitative results at $t = 0$ s should be viewed with healthy skepticism. At other times, the structural changes are gradual enough for our perturbation theory to be reliable.

In this paper, the major sources and sinks of energy considered are nuclear burning, neutrino losses, and losses by coupling to outward propagating p-waves (Lai 2000b). Since losses by radiation is overwhelmed by neutrino emission, perturbations in the radiative flux is ignored. Throughout the Fe core, neutrino losses dominate over energy deposition. Only in the Si- and O-burning shells do nuclear reactions allow the ϵ -mechanism to operate. For the typical g-mode with its largest amplitudes in the center, neutrino losses will dominate in eq. (21), resulting in stability. However, potentially unstable modes are those that are trapped mostly in the outer part of the core near or in the Si-burning region by the discontinuities in entropy, Y_e , and density (Lai 2000b).

4. Results

The results of our analysis are summarized in Table 2, which lists all unstable modes found, and Figs. 4-11, which are described in detail below. Even though we did find modes for $\ell = 1, 2, 3$, and higher ℓ s, we present the results only for $\ell = 1, 2$, and 3 in Table 2. since the trends at higher ℓ s are adequately demonstrated with the set presented in this paper. In general, the most interesting spherical harmonics to

consider are those with odd ℓ , or those with a top-bottom asymmetry. However even ℓ s are interesting as well, as the nonlinear evolution of the perturbations into a kick may be triggered by any low order ℓ . Since the dipole, $\ell = 1$, spherical harmonic most closely resembles the desired kick geometry, we focus in this section on $\ell = 1$, with peripheral mention of $\ell = 2$ and 3.

Stable and unstable modes are found in all progenitor models. Figures 4 and 5 display the propagation diagram for the 13 M_\odot and 30 M_\odot models, at $t = 5$ s before the commencement of collapse. These diagrams represent modes of the compact and extended profiles, respectively. Note again, the spikes resulting from Y_e and ρ discontinuities in P_{Brunt} and the existence of a resonance cavity confined by O-shell convection in the 13 M_\odot model (Fig. 4). Because the O shell is farther out in mass for the more massive 30 M_\odot model (Fig. 5), the density and pressure profiles are more relevant in defining the resonant region. In both figures each horizontal line corresponds to a specific mode; the shading encodes $|\tilde{\xi}|^2$. Dark and lighter shading signify low and high displacement, respectively, while blues denote stable modes and reds identify the unstable modes. Figures 4 and 5 show that there are many more stable modes than unstable modes, which is true for all models at all times and for all ℓ s. We also identify two classes of g-modes, inner-core and outer-core g-modes. Inner-core g-modes have their greatest displacements toward the center and diminish with radius. Their spacing in $\log_{10}(\text{Period})$ systematically decreases with increasing period and increasing number of half-wavelengths, n . In contrast outer-core g-modes do *not* have their greatest amplitude in the center. They are trapped by discontinuities between the fossil Fe core and the O shell in the case of the 13 M_\odot model and within the Si burning shell in the case of the 30 M_\odot model. Similar trapping exists for all other progenitors we consider.

Less than half of the outer-core g-modes are modes trapped entirely under the spikes (i.e. surface g-modes). While these modes satisfy the adiabatic linear oscillation equations, their physical significance is not well constrained. Their eigenfunctions and eigenfrequencies depend on the spike widths and heights, which in turn depend upon the interface between convective and radiative regions in mixing-length theory. However, the results and conclusions we present in this paper are not predicated on their character or existence.

A sample of inner-core g-modes for the 13 M_\odot , $t = 5$ s, model with $\ell = 1$ is plotted versus interior mass in Fig. 6. The decreasing envelope of the eigenfunction and systematic increase in period with increasing half-wavelengths, n , is well explained by a WKB analysis (Unno et al. 1989). The quantization condition, $n\pi = \int k_r dr$, integrated over an appropriate resonant cavity, for g-waves gives

$$\omega_R = \frac{[\ell(\ell+1)]^{1/2}}{n\pi} \int_{cavity} \frac{N}{r} dr. \quad (25)$$

Numerically, the inner core frequencies are proportional to $[\ell(\ell+1)]^{1/2}/n$, and integrating eq. (25) over the appropriate resonance cavity gives approximately the same value. Following the conservation of wave flux arguments in Goldreich & Wu (1999), the envelope for the arbitrarily scaled amplitudes of ξ_r/R and ξ_h/R in Fig. 6 also correspond with those from the WKB analysis. In contrast, a simple WKB analysis fails to predict either the shape or the period of the outer-core g-mode shown in Fig 7. Instead, this mode's period and large displacement farther out in mass are determined by both resonance in the overall cavity and resonant trapping between discontinuities in density, Y_e , and entropy.

In the context of losses and gains in energy, Fig. 8 displays $|\tilde{\xi}|^2$ versus interior mass for two representative inner-core g-modes (top panel) and an outer-core g-mode (bottom panel) for the 13 M_\odot , $t = 5$ s model for $\ell = 1$, in addition to ϵ_{nuc} and ϵ_ν in $\text{erg g}^{-1} \text{s}^{-1}$. Figure 9 presents similar information for the 30 M_\odot model. The overlap of $|\tilde{\xi}|^2$ with ϵ_{nuc} and ϵ_ν is an excellent diagnostic proxy for the integrand in the work integral (eq. (18)). Clearly, neutrino losses dominate the work integral for the case of inner-core g-modes in both

models. For the particular outer-core g-modes plotted for the $13 M_{\odot}$ and $30 M_{\odot}$ progenitors in the bottom panels of Figs. 8 and 9, respectively, the large amplitude in the Si-burning region allows for instability. While all outer-core g-modes in Fig. 5 are unstable, two of the three $13 M_{\odot}$ outer-core g-modes in Fig. 4 are stabilized by neutrino and acoustic losses. In general, at least one outer-core g-mode has the requisite radial perturbation distribution to be unstable.

The growth timescales versus period for $\ell = 1, 2$, and 3 , $t = 60, 30, 25, 20, 15, 10, 5, 2, 1$, and 0 s before the onset of collapse are plotted for $11 M_{\odot}$, $13 M_{\odot}$, and $30 M_{\odot}$ models in Figs. 12, 10, and 11, respectively. As expected, these figures illustrate that for higher ℓ the periods are smaller. Even though we find many unstable modes for the $11 M_{\odot}$ we do not find clear trends in the τ versus period plane. In contrast, as represented by the $13 M_{\odot}$ and $30 M_{\odot}$ models, all other masses we consider demonstrate a distinct trend. The arrows in Figs. 10 and 11 indicate the direction in which the modes evolve with time in the τ versus period plane. Specifically, later models are more compact and have shorter period oscillations. In addition, the later, more compact, models have slightly higher densities and temperatures in the burning regions, thereby dramatically increasing the burning rates and decreasing τ in Figs. 10 and 11. Also note that at no point in any of the models are the growth timescales shorter than the times until the start of collapse. These trends continue to the onset of collapse, which is marked on Figs. 10 and 11 with red symbols. In fact, for the latest models, $t = 0$ s and 1 s before the start of collapse, τ becomes comparable to the period, calling into question the assumption in §2.1 of small nonadiabatic effects. While dramatic changes imposed by dynamical collapse and implosive burning for the $t = 0$ s models make the effects listed above more pronounced, the qualitative trends highlighted still obtain for the $t = 0$ s models.

For all unstable modes found Table 2 lists the progenitor mass, time until onset of collapse, the period, growth timescale, τ , and the contributions, τ_{nuc} , τ_{ν} , and τ_{leak} . From tens of minutes before commencement of collapse until collapse itself, unstable modes exist in *all* progenitor models. However, at every evolutionary stage the timescale for growth is an order-of-magnitude or two longer than the time until onset of collapse. The rates of growth or decay we derive are too long compared to the time to onset of collapse to significantly alter the mode amplitudes. It seems that even though the ϵ -mechanism is present in the later evolutionary stages of the cores of massive stars, the timescales imply that its effect is not large.

4.1. Analytic Estimates

Consistently, we find that the timescales for growth are longer than the time until the onset of collapse. As such the ϵ -mechanism is not able to significantly affect the amplitudes of the unstable g-modes. Hence, our evaluation of the successfulness of the ϵ -mechanism depends upon the validity of the timescale calculations. In this section we corroborate, with an analytic estimate for τ_{nuc} , our numerical evaluations for the growth timescales.

W_j , given by eq. (18), is the rate of energy gained or lost, and E_W , eq. (23), is the energy in the mode. Assuming the region where nuclear burning interacts with a growing mode is small and the mode itself may be represented by a top-hat function located entirely and only within the burning region with maximum displacement $\Delta r/r$, then the integrand in eq. (18) is roughly constant. Therefore,

$$W_j \sim \frac{\pi}{\omega_R} \epsilon_j \epsilon_{jT} \left(\frac{\delta T}{T} \right)^2 \frac{\Delta M}{4\pi}, \quad (26)$$

and eq. (19), simplifies to

$$\frac{\delta T}{T} \sim V \nabla_{ad} \left(\frac{\Delta r}{r} \right). \quad (27)$$

As a harmonic oscillation, g-modes are the oscillations of isodensity contours about their equilibrium positions in hydrostatic equilibrium. The harmonic potential is $U \sim \frac{1}{2} \partial^2 \phi_{eff} / \partial r^2 x^2$, where $x = \Delta r e^{i\omega t}$. From $\vec{\nabla} \phi = \vec{\nabla} P / \rho$, we get $\phi_{eff} \sim \phi \sim P / \rho \sim GM_r / r$. Hence, the potential energy, u , is given by

$$u \sim \frac{GM_r}{r} \left(\frac{x}{r} \right)^2. \quad (28)$$

Since $E_W = 2 \int \langle u \rangle dM_r$, where $\langle \rangle$ denotes the time average over one period of oscillation, then

$$E_W \sim \frac{GM_r}{r} \left(\frac{\Delta r}{r} \right)^2 \frac{\Delta M}{4\pi}. \quad (29)$$

Finally, taking the ratio of eq. (29) and eq. (26) gives a rough estimate for τ :

$$\tau_{nuc} = \frac{4\pi E_W}{\omega_R W_{nuc}} \sim 4 \frac{P/(\rho V)}{\epsilon_{nuc} \epsilon_{nucT} \nabla_{ad}^2}, \quad (30)$$

In the burning region, for the $30 M_\odot$ $t = 5$ s model and the 8.67 s, $\ell = 1$ mode, $P/\rho \sim 2.2 \times 10^{17}$ erg g $^{-1}$, $\epsilon_{nuc} \epsilon_{nucT} \sim 2 \times 10^{16}$ erg g $^{-1}$ s $^{-1}$, $\nabla_{ad} \sim 1/4$, and $V \sim 2$, giving $\tau_{nuc} \sim 320$ s from eq. (30). The numerical solution in Table 2 is $\tau_{nuc} = 328$ s. Similarly for the 8.45 s, $\ell = 1$ mode of the $13 M_\odot$ progenitor model at $t = 1$ s, $P/\rho \sim 1.4 \times 10^{17}$ erg g $^{-1}$, $\epsilon_{nuc} \epsilon_{nucT} \sim 10^{17}$ erg g $^{-1}$ s $^{-1}$, $\nabla_{ad} \sim 1/4$, and $V \sim 3$, giving $\tau_{nuc} \sim 30$ s from eq.(30). The numerical solution (Table 2) is $\tau_{nuc} = 15.5$ s. That the simple analytic arguments and estimates approximately reproduce the numerical results is reassuring. Even though the nuclear rates increase toward later times, at no time is this trend enough to cause significant growth prior to collapse.

5. Summary and Conclusions

For all progenitors, we find stable and unstable g-modes with oscillation periods in the range from ~ 1 to ~ 10 seconds. The stable g-modes are often concentrated in the inner core and are stabilized by neutrino emission. Unstable g-modes on the other hand are trapped in the outer radii of the core by discontinuities in S , density, and Y_e . Their typical growth timescales determined numerically and analytically range from 10s to 10,000s of seconds, which are long compared to the time until the start of collapse. Therefore, we conclude that the ϵ -mechanism is an unlikely source for large perturbations in the progenitor prior to the onset of collapse.

There are several caveats to our conclusion. Our results are for a set of 1-D nonrotating models from Rauscher et al. (2002) and Woosley et al. (2002). Rotation in the late stages of massive stellar evolution may significantly effect the structure of the star prior to collapse (Heger, Langer, & Woosley 2000; Heger, Woosley, & Langer 2003), thereby altering the analysis in this paper. However, with modest Fe core rotation periods ($\gtrsim 10$ s) we expect little deviation from our results, and the simple energy arguments in §4.1 should hold. We also have not considered a different suite of progenitor models (Nomoto & Hashimoto 1988; Limongi & Chieffi 2003), which may have different eigenmodes. In addition, calculating full 3-D, non-linear, dynamical convection with nuclear reactions during the final stages of massive star evolution is a task for the future; the progenitors and their g-modes may be significantly different than assumed or calculated here.

We also have not considered coupling between convective modes and g-modes, which provides an excellent mechanism for the excitation of the 5-minute p-modes in the Sun (Goldreich & Kumar 1990). In such analyses, the amplitudes of the modes are estimated by assuming steady state is achieved in the nonlinear time-dependent amplitude equations. However, the short timescales until the onset of collapse would violate the assumption of steady state and invalidate such analyses. More importantly, it would be unlikely that the short timescales until the onset of collapse would allow for significant excitation of g-modes by convection.

On the other hand, the growth of perturbations in the supersonic regions during collapse does occur (Lai 2000a; Lai & Goldreich 2000). Because we have not ruled out all possible sources of perturbations prior to collapse, asymmetries in the progenitor may still be relevant in producing the largest kicks. For example, convection in the last stages of evolution is often quite vigorous and may have Mach numbers in the range 0.1 to 0.2 and density perturbations, $\delta\rho/\rho$, in the range 0.01 to 0.05 (Bazan & Arnett 1998). These perturbations may indeed be sufficient to produce the observed kicks (Burrows & Hayes 1996).

In performing a stellar pulsational and stability analysis of the late-time cores of massive stars, we have identified many stable and unstable modes. We note that stability is predominantly determined by the neutrino losses or energy deposition by nuclear reactions. Compared with the time until the onset of collapse, the timescales for growth and decay are long. In §4.1, we argue that the long growth timescales (compared with the time until the start of collapse) are confirmed by energetic arguments. We suggest that the ϵ -mechanism for g-mode growth does not generate the requisite perturbations prior to collapse needed to stimulate large kicks during the supernova explosion. Therefore, we conclude that if the hydrodynamic mechanism in combination with progenitor perturbations is to succeed in explaining neutron star kicks other sources of seed perturbations must be investigated.

We thank Phil Arras, Martin Pessah, Tony Piro, Casey Meakin, Stan Woosley, Dong Lai, and Chris Fryer for helpful discussions. Support for this work is provided in part by the Scientific Discovery through Advanced Computing (SciDAC) program of the DOE, grant number DE-FC02-01ER41184. A.H. performed this work under the auspices of the U.S. Department of Energy at the Los Alamos National Laboratory operated by the University of California under contract No. W-7405-ENG-36. The LANL report number for this article is LA-UR-04-3513. J.W.M. would like to thank the Joint Institute for Nuclear Astrophysics (JINA) for providing a graduate fellowship.

REFERENCES

- Arzoumanian, Z., Chernoff, D. F., & Cordes, J. M. 2002, *ApJ*, 568, 289
- Bazan, G., & Arnett, D. 1998, *ApJ*, 496, 316
- Burrows, A., & Hayes, J. 1996, *Physical Review Letters*, 76, 352
- Burrows, A., Hayes, J., & Fryxell, B. A. 1995, *ApJ*, 450, 830
- Christensen-Dalsgaard, J., Dappen, W., Ajukov, S. V., Anderson, E. R., Antia, H. M., Basu, S., Baturin, V. A., Berthomieu, G., et al., 1996, *Science*, 272, 1286
- Cordes, J. M., & Chernoff, D. F. 1998, *ApJ*, 505, 315
- Cordes, J. M., Romani, R. W., & Lundgren, S. C. 1993, *Nature*, 362, 133

- Cordes, J. M., Wasserman, I., & Blaskiewicz, M. 1990, *ApJ*, 349, 546
- Dewey, R. J., & Cordes, J. M. 1987, *ApJ*, 321, 780
- Dewi, J. D. M., & van den Heuvel, E. P. J. 2004, *MNRAS*, 349, 169
- Fryer, C., Burrows, A., & Benz, W. 1998, *ApJ*, 496, 333
- Fryer, C., & Kalogera, V. 1997, *ApJ*, 489, 244
- Goldreich, P., & Kumar, P. 1990, *ApJ*, 363, 694
- Goldreich, P., Lai, D., & Sahriling, M. 1997, in *Unsolved Problems in Astrophysics*, ed. J. Bahcall & J. Ostriker (Princeton, NJ: Princeton University Press, 1997.)
- Goldreich, P., & Wu, Y. 1999, *ApJ*, 511, 904
- Hansen, B. M. S., & Phinney, E. S. 1997, *MNRAS*, 291, 569
- Heger, A., Langer, N., & Woosley, S. E. 2000, *ApJ*, 528, 368
- Heger, A., Woosley, S. E., & Langer, N. 2003, in *IAU Symposium*, 357
- Janka, H.-T., & Müller, E. 1994, *A&A*, 290, 496
- Kalogera, V. 1997, *PASP*, 109, 1394
- Kalogera, V., & Webbink, R. F. 1998, *ApJ*, 493, 351
- Kaspi, V. M., Bailes, M., Manchester, R. N., Stappers, B. W., & Bell, J. F. 1996, *Nature*, 381, 584
- Kramer, M. 1998, *ApJ*, 509, 856
- Kumar, P., & Quataert, E. J. 1997, *ApJ*, 479, L51
- Lai, D. 1996, *ApJ*, 466, L35
- . 2000a, *ApJ*, 540, 946
- . 2000b, *astro-ph/0312265*
- Lai, D., Bildsten, L., & Kaspi, V. M. 1995, *ApJ*, 452, 819
- Lai, D., & Goldreich, P. 2000, *ApJ*, 535, 402
- Limongi, M., & Chieffi, A. 2003, *ApJ*, 592, 404
- Lorimer, D. R., Bailes, M., & Harrison, P. A. 1997, *MNRAS*, 289, 592
- Lyne, A. G., & Lorimer, D. R. 1994, *Nature*, 369, 127
- Nomoto, K., & Hashimoto, M. 1988, *Physics Reports*, 163, 13
- Rauscher, T., Heger, A., Hoffman, R. D., & Woosley, S. E. 2002, *ApJ*, 576, 323
- Scheck, L., Plewa, T., Janka, H.-T., Kifonidis, K., & Müller, E. 2004, *Physical Review Letters*, 92, 011103

- Unno, W., Osaki, Y., Ando, H., Saio, H., & Shibahashi, H. 1989, *Nonradial oscillations of stars* (Nonradial oscillations of stars, Tokyo: University of Tokyo Press, 1989, 2nd ed.)
- Verbunt, F., & van den Heuvel, E. P. J. 1995, in *X-ray binaries*, ed. W. H. G. Lewin, J. van Paradijs, & E. P. J. van den Heuvel (Cambridge Astrophysics Series, Cambridge, MA: Cambridge University Press)
- Wex, N., Kalogera, V., & Kramer, M. 2000, *ApJ*, 528, 401
- Willems, B., & Kalogera, V. 2004, *ApJ*, 603, L101
- Woosley, S. E., Heger, A., & Weaver, T. A. 2002, *Reviews of Modern Physics*, 74, 1015

Table 1. Structural Boundaries

Mass (M_{\odot}) ¹	Fossil Core (M_{\odot}) ²	Fe Core (M_{\odot}) ³	O Base (M_{\odot}) ⁴
11	0.83	1.22 (C)	1.36(C)
13	0.98	1.33 (R)	1.44(C)
15	1.05	1.41 (R)	1.74(C)
20	0.99	1.46 (R)	1.60(C)
30	1.06	1.45 (R)	2.03(C)
35	0.96	1.47 (M)	1.66(C)
40	0.97	1.54 (R)	1.76(C)

¹The initial mass of the model.

²The location of the fossil Fe core, which was formed by convective core Si burning, at 5 s before collapse.

³The location of the base of the Si burning shell or the top of the Fe core, which includes the fossil Fe core and the more recent ashes from the Si burning shell. A C indicates that the shell is convective, R indicates that it is radiative, and M indicates that the shell is radiative in its inner portion and convective in its outer portion.

⁴The location of the base of the O burning shell.

Table 2. Growing Modes

Mass (M_\odot) ¹	t (s) ²	Period (s) ³	τ (s) ⁴	$1/\tau_{nuc}$ (s ⁻¹) ⁵	$-1/\tau_\nu$ (s ⁻¹) ⁶	$-1/\tau_{leak}$ (s ⁻¹) ⁷
$\ell = 1^8$						
11	0	2.21	1.23×10^1	1.60×10^{-1}	6.66×10^{-2}	1.23×10^{-2}
-	1	7.63	5.93×10^2	6.62×10^{-3}	4.93×10^{-3}	~ 0
-	1	4.37	1.20×10^2	1.52×10^{-2}	6.87×10^{-3}	2.20×10^{-5}
-	1	3.04	5.49×10^1	2.87×10^{-2}	6.40×10^{-3}	4.12×10^{-3}
-	1	2.74	1.86×10^2	2.56×10^{-2}	6.30×10^{-3}	1.39×10^{-2}
-	5	4.97	1.85×10^2	7.09×10^{-3}	1.68×10^{-3}	1.56×10^{-5}
-	5	3.53	2.56×10^2	7.96×10^{-3}	2.02×10^{-3}	2.03×10^{-3}
-	30	9.14	3.47×10^2	3.79×10^{-3}	9.07×10^{-4}	~ 0
-	30	6.24	5.69×10^2	3.07×10^{-3}	1.31×10^{-3}	~ 0
-	30	5.75	9.77×10^1	1.11×10^{-2}	8.26×10^{-4}	~ 0
-	30	4.96	8.20×10^2	2.68×10^{-3}	1.44×10^{-3}	1.87×10^{-5}
-	30	4.09	1.83×10^2	7.23×10^{-3}	9.63×10^{-4}	8.07×10^{-4}
-	30	3.62	1.30×10^3	4.14×10^{-3}	1.15×10^{-3}	2.22×10^{-3}
-	60	9.80	6.74×10^2	2.09×10^{-3}	6.11×10^{-4}	~ 0
-	60	6.80	7.24×10^2	2.19×10^{-3}	8.11×10^{-4}	~ 0
-	60	6.37	2.34×10^2	4.89×10^{-3}	6.15×10^{-4}	~ 0
-	60	4.48	8.15×10^2	2.36×10^{-3}	6.85×10^{-4}	4.50×10^{-4}
13	0	4.44	8.59×10^0	2.54×10^{-1}	1.37×10^{-1}	6.46×10^{-6}
-	0	4.34	4.70×10^{-1}	2.15×10^0	2.32×10^{-2}	9.40×10^{-5}
-	1	8.42	1.55×10^1	6.65×10^{-2}	2.19×10^{-3}	4.82×10^{-6}
-	1	5.59	3.47×10^1	3.24×10^{-2}	3.38×10^{-3}	1.42×10^{-4}
-	5	9.50	7.90×10^2	2.32×10^{-3}	1.05×10^{-3}	4.20×10^{-6}
15	0	4.59	7.13×10^{-1}	1.43×10^0	1.54×10^{-3}	2.61×10^{-2}
-	1	8.39	3.15×10^1	3.18×10^{-2}	6.32×10^{-5}	~ 0
-	1	5.23	5.64×10^1	5.02×10^{-2}	6.05×10^{-4}	3.19×10^{-2}
-	5	8.66	1.37×10^2	7.35×10^{-3}	4.82×10^{-5}	~ 0
-	30	9.15	4.43×10^2	2.30×10^{-3}	3.88×10^{-5}	~ 0
-	30	6.62	9.75×10^2	1.42×10^{-3}	3.93×10^{-4}	~ 0
-	60	9.52	6.31×10^2	1.63×10^{-3}	4.40×10^{-5}	~ 0
-	60	7.03	9.44×10^2	1.45×10^{-3}	3.92×10^{-4}	~ 0
-	600	11.04	9.68×10^5	6.84×10^{-5}	6.73×10^{-5}	~ 0
-	3600	24.28	5.48×10^4	7.68×10^{-5}	5.86×10^{-5}	~ 0
-	3600	16.47	9.99×10^4	5.89×10^{-5}	4.89×10^{-5}	~ 0
-	3600	13.00	3.40×10^5	2.40×10^{-5}	2.11×10^{-5}	~ 0
20	1	10.03	3.61×10^1	2.94×10^{-2}	1.65×10^{-3}	1.95×10^{-5}

Table 2—Continued

Mass (M_\odot) ¹	t (s) ²	Period (s) ³	τ (s) ⁴	$1/\tau_{nuc}$ (s ⁻¹) ⁵	$-1/\tau_\nu$ (s ⁻¹) ⁶	$-1/\tau_{leak}$ (s ⁻¹) ⁷
-	1	6.77	1.77×10^2	9.49×10^{-3}	3.68×10^{-3}	1.43×10^{-4}
-	5	11.14	2.91×10^2	4.18×10^{-3}	7.44×10^{-4}	5.11×10^{-6}
25	0	5.86	7.29×10^{-1}	1.38×10^0	4.03×10^{-3}	~ 0
-	1	10.70	2.89×10^1	3.79×10^{-2}	3.27×10^{-3}	~ 0
-	1	7.09	1.74×10^1	5.96×10^{-2}	2.20×10^{-3}	~ 0
-	1	6.74	1.17×10^2	1.34×10^{-2}	4.85×10^{-3}	~ 0
-	5	11.30	3.97×10^2	3.91×10^{-3}	1.39×10^{-3}	~ 0
-	5	7.88	2.54×10^2	5.04×10^{-3}	1.10×10^{-3}	~ 0
-	30	8.71	2.59×10^3	1.12×10^{-3}	7.33×10^{-4}	~ 0
-	60	9.18	1.01×10^4	7.30×10^{-4}	6.31×10^{-4}	~ 0
-	3600	17.25	8.35×10^5	6.13×10^{-5}	6.01×10^{-5}	~ 0
30	0	5.35	2.28×10^0	4.41×10^{-1}	3.31×10^{-3}	~ 0
-	1	7.51	2.44×10^1	4.18×10^{-2}	8.26×10^{-4}	~ 0
-	5	8.67	4.23×10^2	3.04×10^{-3}	6.76×10^{-4}	~ 0
-	30	9.79	3.84×10^3	7.83×10^{-4}	5.23×10^{-4}	~ 0
-	3600	16.13	5.74×10^6	3.21×10^{-5}	3.20×10^{-5}	~ 0
35	0	5.09	3.49×10^1	9.27×10^{-2}	6.41×10^{-2}	1.49×10^{-5}
-	0	4.82	5.28×10^{-1}	1.90×10^0	6.93×10^{-3}	1.08×10^{-3}
-	1	7.99	1.81×10^2	8.57×10^{-3}	3.05×10^{-3}	~ 0
-	1	7.60	1.35×10^2	1.06×10^{-2}	3.16×10^{-3}	~ 0
-	1	5.85	5.22×10^1	2.14×10^{-2}	2.20×10^{-3}	~ 0
-	5	8.36	9.90×10^2	2.06×10^{-3}	1.05×10^{-3}	~ 0
-	5	6.44	1.09×10^3	2.14×10^{-3}	1.22×10^{-3}	~ 0
-	30	9.19	5.03×10^3	7.07×10^{-4}	5.09×10^{-4}	~ 0
-	60	9.70	6.22×10^3	5.61×10^{-4}	4.00×10^{-4}	~ 0
40	0	5.95	5.45×10^1	6.82×10^{-2}	4.98×10^{-2}	1.83×10^{-5}
-	0	5.47	5.43×10^{-1}	1.85×10^0	7.20×10^{-3}	1.55×10^{-3}
-	1	9.00	7.88×10^1	1.60×10^{-2}	3.31×10^{-3}	~ 0
-	1	8.56	3.63×10^1	3.03×10^{-2}	2.81×10^{-3}	~ 0
-	1	7.39	4.46×10^3	4.74×10^{-3}	4.51×10^{-3}	~ 0
-	1	6.36	5.41×10^1	2.24×10^{-2}	3.47×10^{-3}	5.00×10^{-4}
-	1	5.95	5.62×10^1	2.23×10^{-2}	3.36×10^{-3}	1.11×10^{-3}
-	5	9.45	6.06×10^2	2.55×10^{-3}	8.97×10^{-4}	~ 0
$\ell = 2$						
11	0	1.36	4.55×10^1	1.19×10^{-1}	8.66×10^{-2}	9.96×10^{-3}
-	1	4.47	9.37×10^2	6.07×10^{-3}	5.00×10^{-3}	~ 0

Table 2—Continued

Mass (M_\odot) ¹	t (s) ²	Period (s) ³	τ (s) ⁴	$1/\tau_{nuc}$ (s ⁻¹) ⁵	$-1/\tau_\nu$ (s ⁻¹) ⁶	$-1/\tau_{eak}$ (s ⁻¹) ⁷
-	1	2.63	1.02×10^2	1.57×10^{-2}	5.87×10^{-3}	1.19×10^{-5}
-	1	1.90	1.28×10^2	1.75×10^{-2}	7.99×10^{-3}	1.67×10^{-3}
-	1	1.73	7.23×10^1	3.58×10^{-2}	4.37×10^{-3}	1.76×10^{-2}
-	5	4.82	2.40×10^3	2.28×10^{-3}	1.86×10^{-3}	~ 0
-	5	2.98	1.98×10^2	6.66×10^{-3}	1.59×10^{-3}	1.11×10^{-5}
-	5	2.68	6.02×10^3	2.93×10^{-3}	2.74×10^{-3}	2.73×10^{-5}
-	5	2.21	5.67×10^2	4.89×10^{-3}	2.40×10^{-3}	7.25×10^{-4}
-	5	1.98	1.41×10^3	1.15×10^{-2}	1.31×10^{-3}	9.52×10^{-3}
-	30	5.35	3.45×10^2	3.77×10^{-3}	8.73×10^{-4}	~ 0
-	30	3.77	3.43×10^3	1.70×10^{-3}	1.41×10^{-3}	~ 0
-	30	3.44	8.76×10^1	1.21×10^{-2}	7.12×10^{-4}	~ 0
-	30	3.07	6.34×10^2	2.98×10^{-3}	1.39×10^{-3}	1.02×10^{-5}
-	30	2.55	2.50×10^2	5.46×10^{-3}	1.11×10^{-3}	3.54×10^{-4}
-	30	2.29	2.94×10^2	6.24×10^{-3}	9.68×10^{-4}	1.87×10^{-3}
-	60	5.74	6.82×10^2	2.08×10^{-3}	6.13×10^{-4}	~ 0
-	60	4.10	2.49×10^3	1.30×10^{-3}	8.98×10^{-4}	~ 0
-	60	3.82	1.81×10^2	6.04×10^{-3}	5.00×10^{-4}	~ 0
-	60	2.78	1.21×10^3	1.79×10^{-3}	7.59×10^{-4}	2.04×10^{-4}
-	60	2.50	6.38×10^3	1.79×10^{-3}	7.31×10^{-4}	8.98×10^{-4}
13	0	2.68	2.77×10^0	4.87×10^{-1}	1.26×10^{-1}	9.02×10^{-6}
-	0	2.65	5.43×10^{-1}	1.88×10^0	3.80×10^{-2}	4.10×10^{-5}
-	1	4.99	1.49×10^1	6.93×10^{-2}	2.10×10^{-3}	1.89×10^{-6}
-	1	3.44	3.46×10^1	3.24×10^{-2}	3.41×10^{-3}	6.10×10^{-5}
-	5	5.64	7.10×10^2	2.41×10^{-3}	9.96×10^{-4}	2.04×10^{-6}
15	0	2.85	6.14×10^{-1}	1.64×10^0	1.25×10^{-3}	7.38×10^{-3}
-	0	1.79	1.01×10^1	1.76×10^{-1}	6.39×10^{-2}	1.35×10^{-2}
-	0	1.72	3.76×10^0	3.35×10^{-1}	3.67×10^{-2}	3.26×10^{-2}
-	1	6.16	5.42×10^1	1.85×10^{-2}	3.28×10^{-5}	~ 0
-	1	3.24	1.89×10^1	6.47×10^{-2}	4.80×10^{-4}	1.14×10^{-2}
-	5	6.34	1.75×10^2	5.76×10^{-3}	2.55×10^{-5}	~ 0
-	60	4.34	1.10×10^3	1.24×10^{-3}	3.28×10^{-4}	~ 0
-	3600	14.17	6.48×10^4	7.16×10^{-5}	5.62×10^{-5}	~ 0
-	3600	10.32	1.58×10^5	2.71×10^{-5}	2.08×10^{-5}	~ 0
-	3600	9.11	1.73×10^5	4.80×10^{-5}	4.22×10^{-5}	~ 0
20	1	6.04	3.50×10^1	3.02×10^{-2}	1.65×10^{-3}	9.49×10^{-6}
-	1	4.19	3.43×10^2	7.12×10^{-3}	4.15×10^{-3}	4.97×10^{-5}
25	0	2.38	2.85×10^0	4.67×10^{-1}	7.70×10^{-4}	1.16×10^{-1}
-	1	6.43	3.07×10^1	3.59×10^{-2}	3.39×10^{-3}	~ 0

Table 2—Continued

Mass (M_{\odot}) ¹	t (s) ²	Period (s) ³	τ (s) ⁴	$1/\tau_{nuc}$ (s ⁻¹) ⁵	$-1/\tau_{\nu}$ (s ⁻¹) ⁶	$-1/\tau_{leak}$ (s ⁻¹) ⁷
-	1	4.43	1.52×10^1	6.78×10^{-2}	1.87×10^{-3}	~ 0
-	1	4.24	2.20×10^2	9.57×10^{-3}	5.02×10^{-3}	~ 0
-	5	6.58	1.21×10^3	2.49×10^{-3}	1.67×10^{-3}	~ 0
-	5	4.91	2.32×10^2	5.39×10^{-3}	1.07×10^{-3}	~ 0
-	30	5.41	1.56×10^3	1.17×10^{-3}	5.28×10^{-4}	~ 0
-	60	5.70	8.32×10^3	7.60×10^{-4}	6.40×10^{-4}	~ 0
-	3600	4.59	4.81×10^4	3.23×10^{-5}	1.15×10^{-5}	~ 0
30	0	3.20	2.27×10^0	4.41×10^{-1}	1.12×10^{-3}	~ 0
-	0	1.68	1.49×10^0	7.94×10^{-1}	2.55×10^{-3}	1.21×10^{-1}
-	1	4.52	2.47×10^1	4.12×10^{-2}	6.75×10^{-4}	~ 0
-	5	5.23	4.11×10^2	3.01×10^{-3}	5.74×10^{-4}	~ 0
-	30	5.91	3.37×10^3	7.55×10^{-4}	4.58×10^{-4}	~ 0
35	0	2.98	4.93×10^{-1}	2.03×10^0	5.28×10^{-3}	6.57×10^{-4}
-	1	4.77	2.31×10^2	7.53×10^{-3}	3.20×10^{-3}	~ 0
-	1	4.56	1.34×10^2	1.06×10^{-2}	3.15×10^{-3}	~ 0
-	1	3.63	5.13×10^1	2.17×10^{-2}	2.23×10^{-3}	~ 0
-	1	3.41	2.01×10^3	4.80×10^{-3}	4.30×10^{-3}	~ 0
-	5	5.00	8.02×10^2	2.24×10^{-3}	9.89×10^{-4}	~ 0
-	5	3.99	1.45×10^3	1.96×10^{-3}	1.27×10^{-3}	~ 0
-	30	5.49	4.08×10^3	7.37×10^{-4}	4.92×10^{-4}	~ 0
-	60	5.79	4.78×10^3	5.93×10^{-4}	3.84×10^{-4}	~ 0
40	0	3.44	5.12×10^{-1}	1.96×10^0	6.00×10^{-3}	7.37×10^{-4}
-	0	2.04	1.14×10^1	2.73×10^{-1}	1.27×10^{-3}	1.83×10^{-1}
-	1	5.37	7.42×10^1	1.68×10^{-2}	3.32×10^{-3}	~ 0
-	1	5.14	3.53×10^1	3.11×10^{-2}	2.85×10^{-3}	~ 0
-	1	3.99	6.50×10^1	1.94×10^{-2}	3.74×10^{-3}	2.70×10^{-4}
-	1	3.75	4.21×10^1	2.75×10^{-2}	2.95×10^{-3}	8.16×10^{-4}
-	5	5.68	5.29×10^2	2.75×10^{-3}	8.57×10^{-4}	~ 0
$\ell = 3$						
11	0	0.99	1.10×10^1	1.63×10^{-1}	5.81×10^{-2}	1.35×10^{-2}
-	0	0.88	3.74×10^0	4.71×10^{-1}	1.03×10^{-2}	1.94×10^{-1}
-	1	1.95	1.12×10^2	1.42×10^{-2}	5.20×10^{-3}	2.74×10^{-6}
-	1	1.33	2.69×10^1	4.67×10^{-2}	3.09×10^{-3}	6.43×10^{-3}
-	5	3.49	1.49×10^3	2.34×10^{-3}	1.66×10^{-3}	~ 0
-	5	2.21	2.90×10^2	5.19×10^{-3}	1.73×10^{-3}	1.77×10^{-6}
-	5	2.04	7.05×10^2	3.85×10^{-3}	2.43×10^{-3}	6.93×10^{-6}

Table 2—Continued

Mass (M_\odot) ¹	t (s) ²	Period (s) ³	τ (s) ⁴	$1/\tau_{nuc}$ (s ⁻¹) ⁵	$-1/\tau_\nu$ (s ⁻¹) ⁶	$-1/\tau_{eak}$ (s ⁻¹) ⁷
-	5	1.72	3.69×10^3	2.98×10^{-3}	2.63×10^{-3}	8.16×10^{-5}
-	5	1.53	9.65×10^1	1.46×10^{-2}	1.06×10^{-3}	3.19×10^{-3}
-	30	3.86	3.89×10^2	3.45×10^{-3}	8.84×10^{-4}	~ 0
-	30	2.54	8.66×10^1	1.22×10^{-2}	6.88×10^{-4}	~ 0
-	30	2.34	3.47×10^2	4.18×10^{-3}	1.30×10^{-3}	~ 0
-	30	1.98	3.78×10^2	3.92×10^{-3}	1.22×10^{-3}	4.68×10^{-5}
-	30	1.79	1.43×10^2	8.31×10^{-3}	8.23×10^{-4}	4.93×10^{-4}
-	60	4.15	8.29×10^2	1.86×10^{-3}	6.54×10^{-4}	~ 0
-	60	2.83	1.53×10^2	6.97×10^{-3}	4.27×10^{-4}	~ 0
-	60	2.56	5.36×10^4	9.63×10^{-4}	9.45×10^{-4}	~ 0
-	60	2.16	2.59×10^3	1.23×10^{-3}	8.23×10^{-4}	2.29×10^{-5}
-	60	1.95	7.26×10^2	2.24×10^{-3}	6.45×10^{-4}	2.18×10^{-4}
13	0	2.02	9.43×10^{-1}	1.14×10^0	8.20×10^{-2}	3.31×10^{-6}
-	0	2.01	9.39×10^{-1}	1.15×10^0	8.29×10^{-2}	3.63×10^{-6}
-	0	2.01	9.39×10^{-1}	1.15×10^0	8.29×10^{-2}	3.63×10^{-6}
-	1	3.66	1.41×10^1	7.29×10^{-2}	1.99×10^{-3}	3.30×10^{-7}
-	1	2.65	3.66×10^1	3.09×10^{-2}	3.53×10^{-3}	7.66×10^{-6}
-	5	4.14	6.59×10^2	2.47×10^{-3}	9.52×10^{-4}	3.54×10^{-7}
15	0	2.21	5.65×10^{-1}	1.77×10^0	1.06×10^{-3}	1.26×10^{-3}
-	0	1.42	3.08×10^1	1.02×10^{-1}	6.84×10^{-2}	1.45×10^{-3}
-	0	1.38	4.50×10^0	2.57×10^{-1}	3.07×10^{-2}	4.45×10^{-3}
-	1	2.49	1.31×10^1	7.92×10^{-2}	3.38×10^{-4}	2.56×10^{-3}
-	1	1.67	2.17×10^1	5.90×10^{-2}	1.34×10^{-3}	1.16×10^{-2}
-	5	2.76	1.89×10^2	7.16×10^{-3}	2.20×10^{-4}	1.64×10^{-3}
-	30	3.06	1.05×10^3	1.22×10^{-3}	2.67×10^{-4}	~ 0
-	60	3.26	1.07×10^3	1.20×10^{-3}	2.67×10^{-4}	~ 0
-	3600	10.18	8.41×10^4	6.51×10^{-5}	5.32×10^{-5}	~ 0
-	3600	8.42	2.73×10^5	8.11×10^{-6}	4.45×10^{-6}	~ 0
-	3600	6.95	5.68×10^5	5.03×10^{-5}	4.85×10^{-5}	~ 0
20	1	4.58	6.79×10^1	1.79×10^{-2}	3.14×10^{-3}	7.57×10^{-7}
-	1	4.51	6.96×10^1	1.76×10^{-2}	3.25×10^{-3}	8.71×10^{-7}
-	1	3.35	2.38×10^2	8.13×10^{-3}	3.91×10^{-3}	5.18×10^{-6}
25	0	2.00	2.80×10^0	3.82×10^{-1}	3.23×10^{-4}	2.42×10^{-2}
-	0	1.00	1.17×10^2	1.99×10^{-2}	9.07×10^{-3}	2.28×10^{-3}
-	1	3.45	1.21×10^1	8.42×10^{-2}	1.48×10^{-3}	~ 0
-	1	2.20	2.17×10^2	2.06×10^{-2}	2.23×10^{-3}	1.37×10^{-2}
-	1	2.17	3.40×10^2	1.74×10^{-2}	2.94×10^{-3}	1.15×10^{-2}
-	5	3.81	1.92×10^2	6.24×10^{-3}	1.03×10^{-3}	~ 0

Table 2—Continued

Mass (M_{\odot}) ¹	t (s) ²	Period (s) ³	τ (s) ⁴	$1/\tau_{nuc}$ (s ⁻¹) ⁵	$-1/\tau_{\nu}$ (s ⁻¹) ⁶	$-1/\tau_{leak}$ (s ⁻¹) ⁷
-	30	4.20	2.15×10^3	1.24×10^{-3}	7.70×10^{-4}	~ 0
-	60	4.41	9.52×10^3	7.75×10^{-4}	6.70×10^{-4}	~ 0
-	600	3.18	2.42×10^3	4.36×10^{-4}	2.25×10^{-5}	~ 0
-	3600	3.86	4.35×10^4	3.23×10^{-5}	9.29×10^{-6}	~ 0
30	0	2.36	2.30×10^0	4.35×10^{-1}	6.71×10^{-4}	~ 0
-	0	1.38	1.10×10^0	9.31×10^{-1}	1.52×10^{-3}	2.41×10^{-2}
-	1	3.34	2.44×10^1	4.16×10^{-2}	5.30×10^{-4}	~ 0
-	1	1.66	6.45×10^1	4.43×10^{-2}	4.29×10^{-4}	2.83×10^{-2}
-	5	3.87	3.90×10^2	3.01×10^{-3}	4.51×10^{-4}	~ 0
-	30	4.38	2.59×10^3	7.54×10^{-4}	3.68×10^{-4}	~ 0
35	0	2.30	4.93×10^{-1}	2.03×10^0	2.93×10^{-3}	8.37×10^{-5}
-	1	3.55	6.73×10^3	4.07×10^{-3}	3.92×10^{-3}	~ 0
-	1	3.41	1.11×10^2	1.20×10^{-2}	2.98×10^{-3}	~ 0
-	1	2.79	4.35×10^1	2.49×10^{-2}	1.93×10^{-3}	~ 0
-	1	2.65	2.13×10^4	4.25×10^{-3}	4.20×10^{-3}	~ 0
-	5	3.71	7.14×10^2	2.34×10^{-3}	9.42×10^{-4}	~ 0
-	5	3.07	1.42×10^3	1.94×10^{-3}	1.23×10^{-3}	~ 0
-	30	4.06	6.22×10^3	6.79×10^{-4}	5.18×10^{-4}	~ 0
-	60	4.28	6.63×10^3	5.36×10^{-4}	3.85×10^{-4}	~ 0
-	3600	3.31	1.63×10^5	1.14×10^{-5}	5.26×10^{-6}	~ 0
40	0	1.74	4.63×10^0	2.59×10^{-1}	3.73×10^{-4}	4.29×10^{-2}
-	0	0.98	2.71×10^2	2.07×10^{-2}	1.51×10^{-2}	1.89×10^{-3}
-	1	4.00	1.24×10^2	1.20×10^{-2}	3.90×10^{-3}	~ 0
-	1	3.86	2.85×10^1	3.77×10^{-2}	2.67×10^{-3}	~ 0
-	1	3.55	2.18×10^3	5.41×10^{-3}	4.95×10^{-3}	5.42×10^{-7}
-	1	3.09	4.21×10^1	2.70×10^{-2}	3.22×10^{-3}	6.66×10^{-5}
-	1	2.94	4.82×10^1	2.41×10^{-2}	3.23×10^{-3}	1.16×10^{-4}
-	5	4.25	4.14×10^2	3.18×10^{-3}	7.66×10^{-4}	~ 0
-	5	3.20	3.03×10^3	1.66×10^{-3}	1.22×10^{-3}	1.08×10^{-4}
-	30	4.65	1.90×10^4	4.75×10^{-4}	4.23×10^{-4}	~ 0

¹The initial mass of the model.

²The time before collapse in seconds.

³The period of the particular growing mode.

⁴The growth timescale given by $1/\tau = 1/\tau_{nuc} + 1/\tau_{\nu} + 1/\tau_{leak}$

⁵Inverse of the growth timescale from nuclear burning.

⁶Negative and inverse of the decay timescale due to ν emission.

⁷Negative and inverse of the decay timescale due to acoustic losses to the envelope.

⁸Each row is associated with a specific ℓ given by the header for each section.

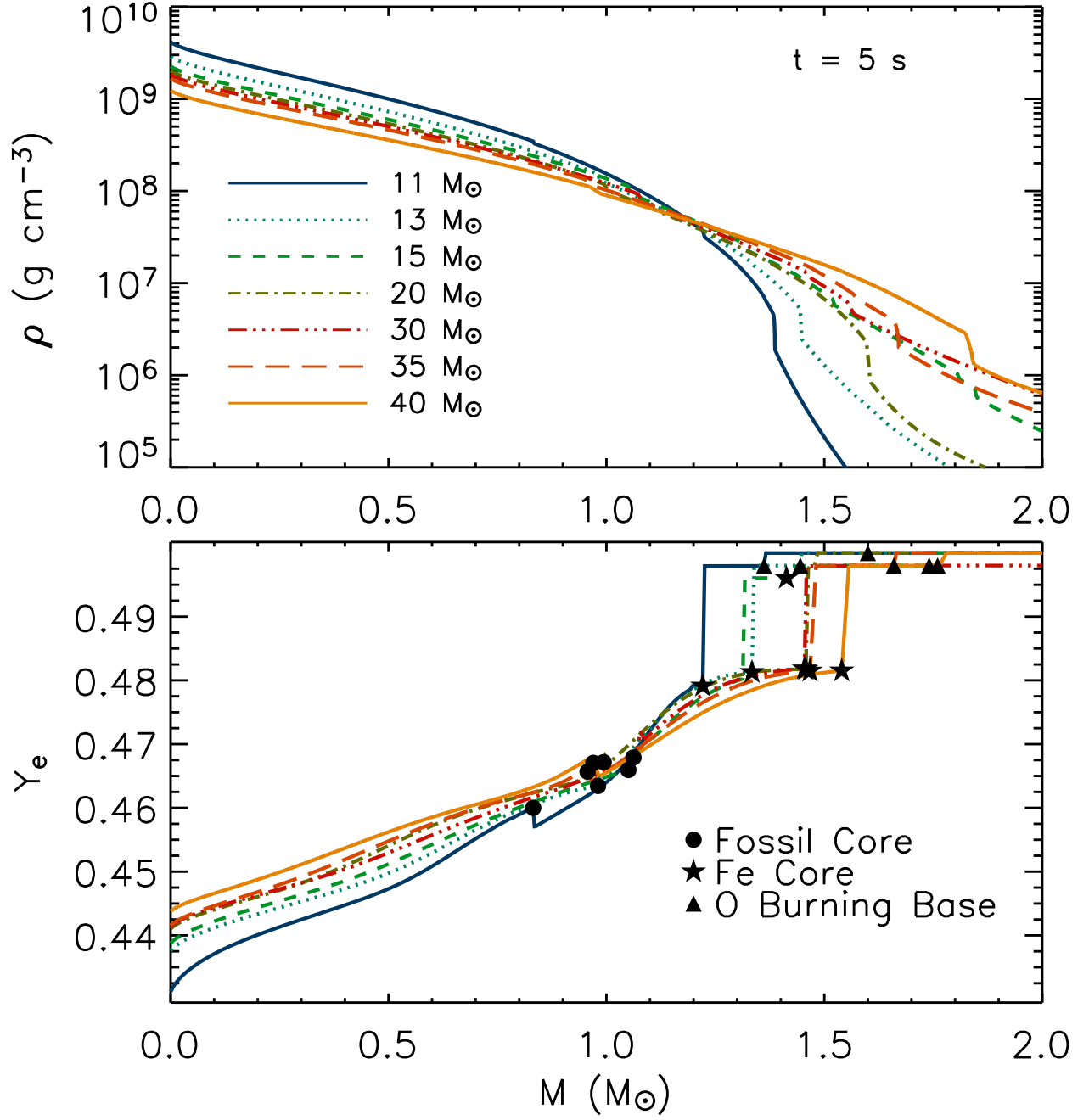


Fig. 1.— Density (top panel) and electron fraction, Y_e , (bottom panel) verses interior mass, M , for the 11 M_{\odot} (solid and dark blue), 13 M_{\odot} (dotted and light blue), 15 M_{\odot} (dashed and green), 20 M_{\odot} (dot-dash and olive green), 30 M_{\odot} (dot-dot-dot-dash and red), 35 M_{\odot} (long dashed and orange), and 40 M_{\odot} (solid orange) models, all at 5 s before the onset of collapse. Note in the top panel that the lower mass models have higher central densities, but that the higher mass models have shallower density gradients. Included on the Y_e plot are points indicating significant features in the star, which greatly affect the modes. Circles represent the farthest extent of the fossil Fe core, which was formed during convective core Si burning. Stars represent the base of the Si burning shell at 5 seconds before the start of collapse (i.e., the extent of the Fe core, including the fossil Fe and the most recent ashes from Si shell burning), which generally aren't convective until collapse. The triangles represent the base of the convective O burning shell

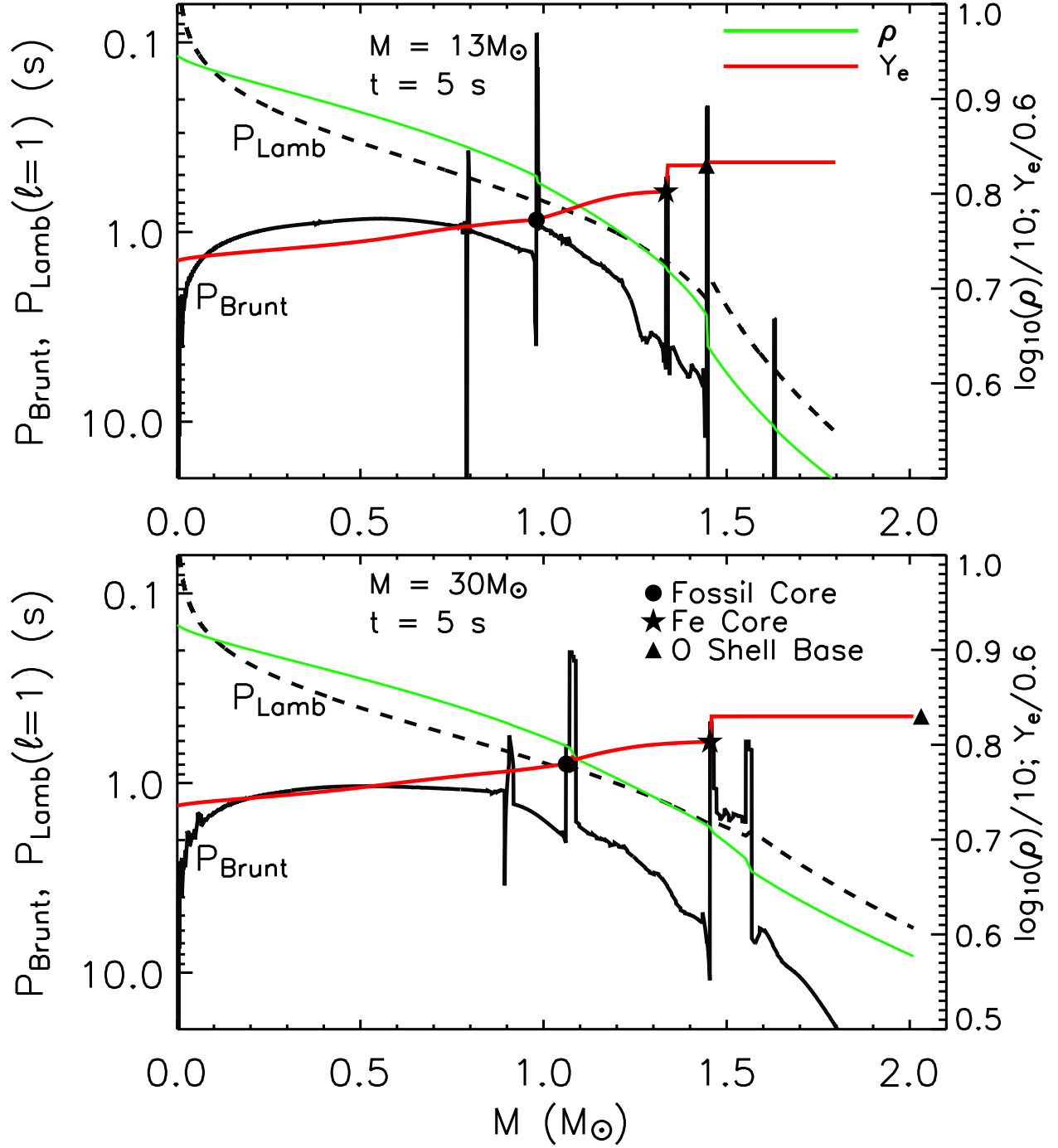


Fig. 2.— Density (solid green) and Y_e (solid red) versus interior mass in comparison to the propagation diagram for the $13 M_\odot$ model at 5 s before the onset of collapse. Usually, the square of the Brunt-Väisälä (N^2) and Lamb (L_ℓ^2) frequencies are plotted. In this case, an equivalent period of oscillation is displayed instead, defined by $P_{\text{Brunt}} = 2\pi/\sqrt{|N^2|}$ and $P_{\text{Lamb}} = 2\pi/\sqrt{|L_\ell^2|}$. The circles, stars, and triangles represent the same structural boundaries as in Fig. 1. The vertical spikes are from discontinuous density and Y_e changes in the profiles and are real. The bottom panel provides the equivalent information for the $30 M_\odot$ model.

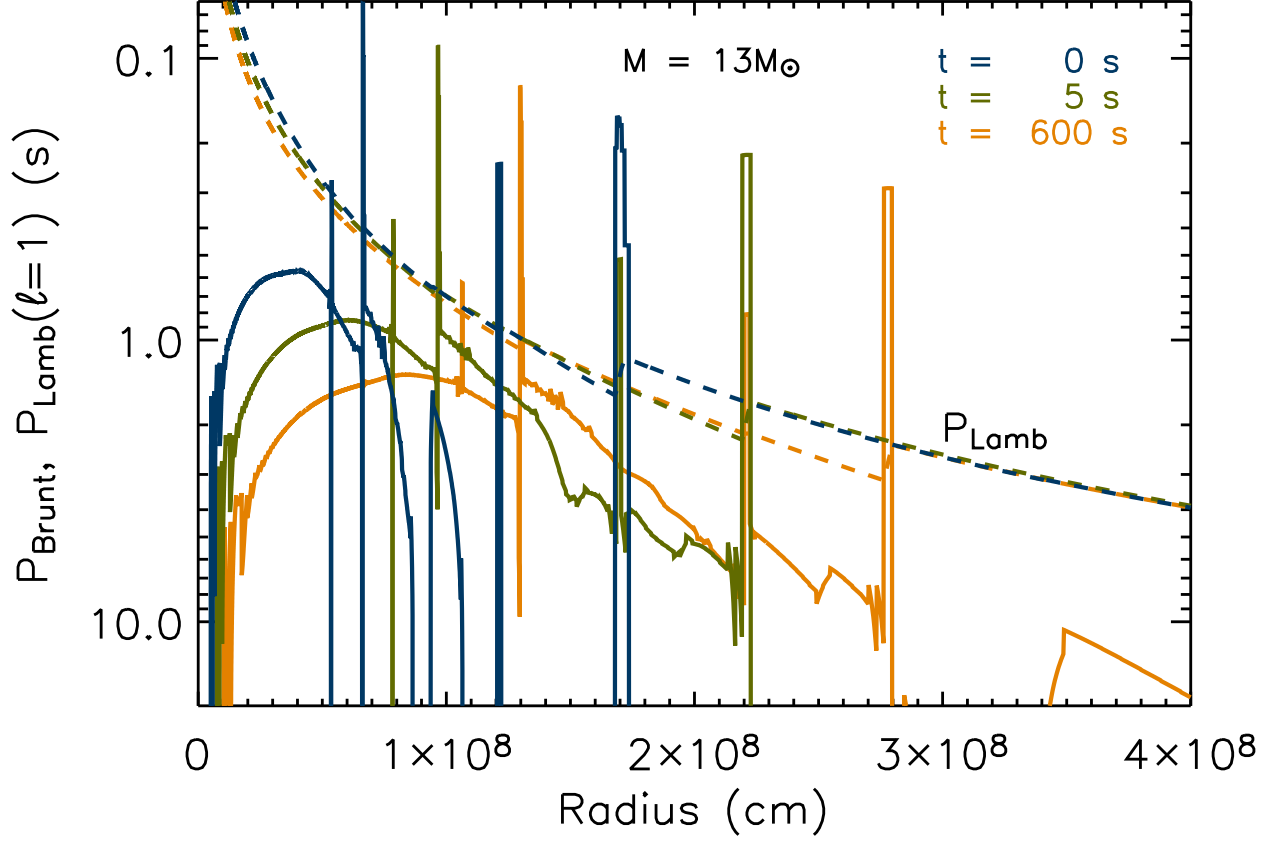


Fig. 3.— A time series of the propagation diagram for the $13 M_{\odot}$ model from 600 s to 0 s before the start of collapse. P_{Brunt} and P_{Lamb} are defined as in Fig. 2. Notice that the evolution abruptly changes for $t = 0$ s. This is due to the dramatic increase in nuclear rates during implosive burning, which causes new regions to become convective in the mixing-length calculation.

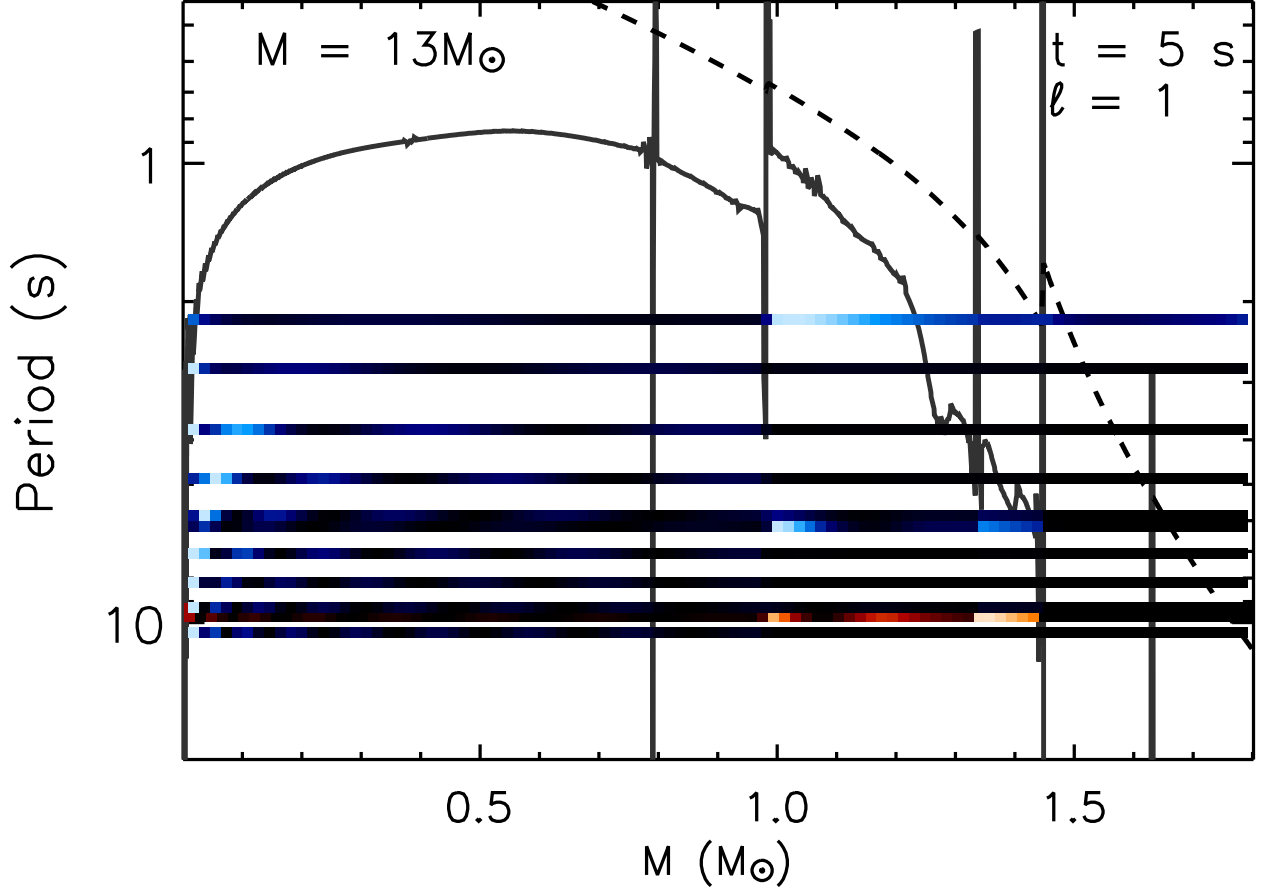


Fig. 4.— The propagation diagram for $\ell = 1$ and the $13 M_{\odot}$ model at 5 s before the onset of collapse with P_{Brunt} (solid) and $P_{Lamb}(\ell = 1)$ (dashed), as defined in Fig. 2. The horizontal lines correspond to each eigenmode and period and are quantized. The shading in the lines is a measure of the magnitudes of the square of the amplitude, $|\xi|^2$. Within a single line brighter portions indicate a higher amplitude while the darker color signifies a lower amplitude. The blues indicate modes which are stable ($\tau < 0$), and the reds correspond to the modes which are unstable ($\tau > 0$).

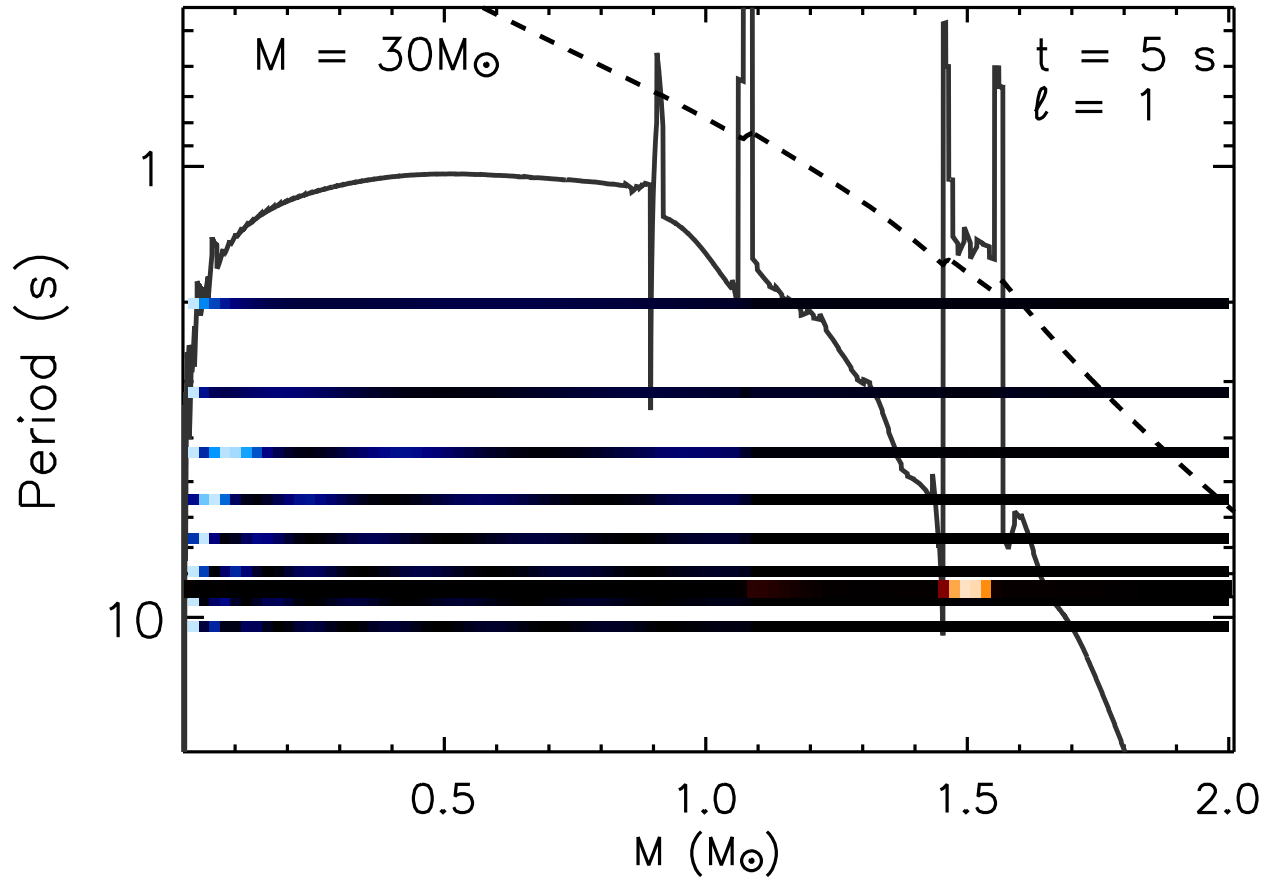


Fig. 5.— This figure is similar to Fig. 4, but for the $30 M_\odot$ model.

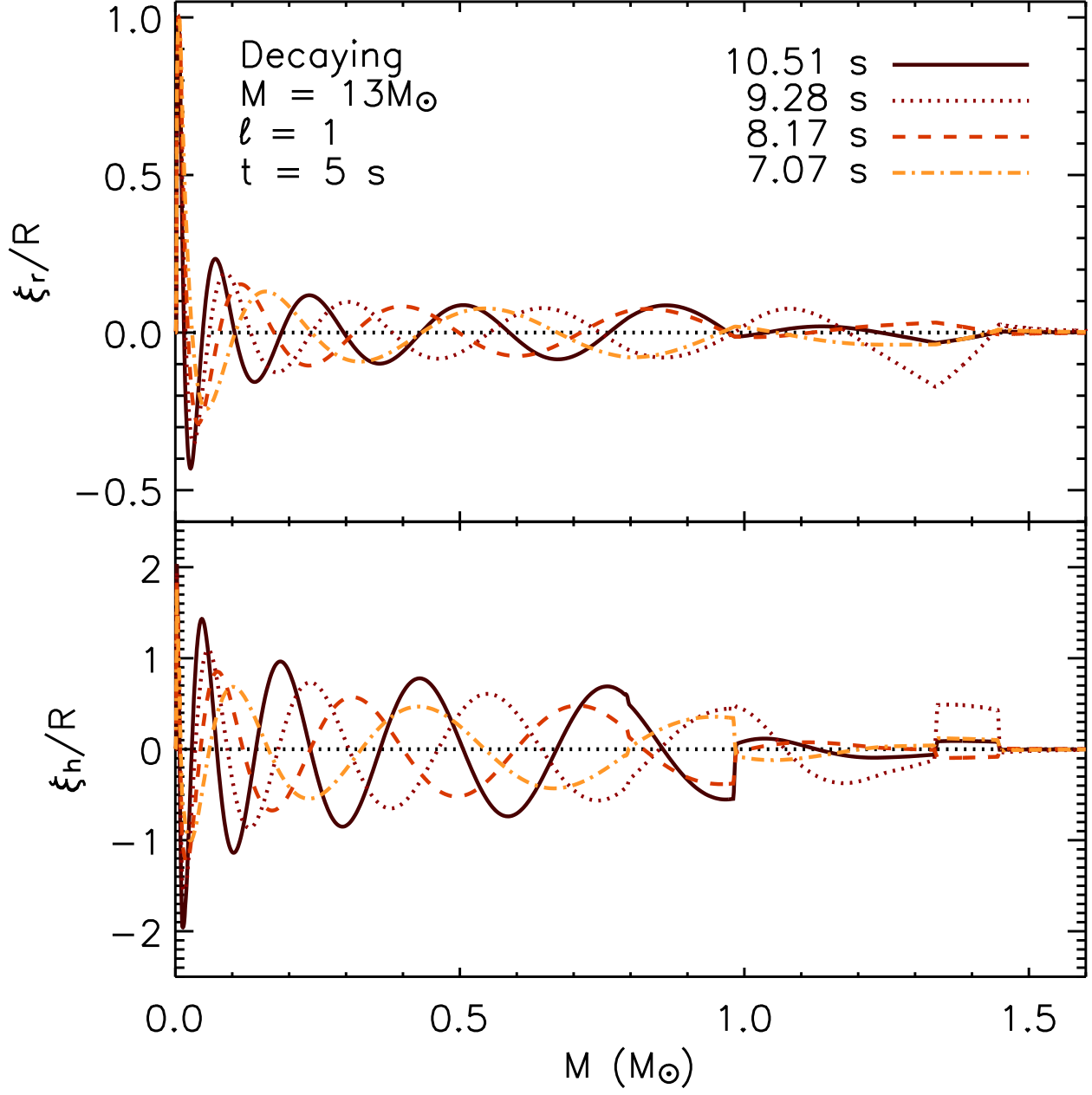


Fig. 6.— The dimensionless eigenfunctions of *stable* g-mode oscillations with periods of 10.51, 9.28, 8.17, and 7.07 s, for $\ell = 1$, $13 M_{\odot}$, and 5 s before the start of collapse. Each mode is distinguished by its period. The top panel plots ξ_r/R , where ξ_r is the radial component of perturbation and R is the calculation domain size. The amplitude is arbitrarily scaled to 1.0 at its peak value. The bottom panel plots the corresponding horizontal amplitude, ξ_h/R .

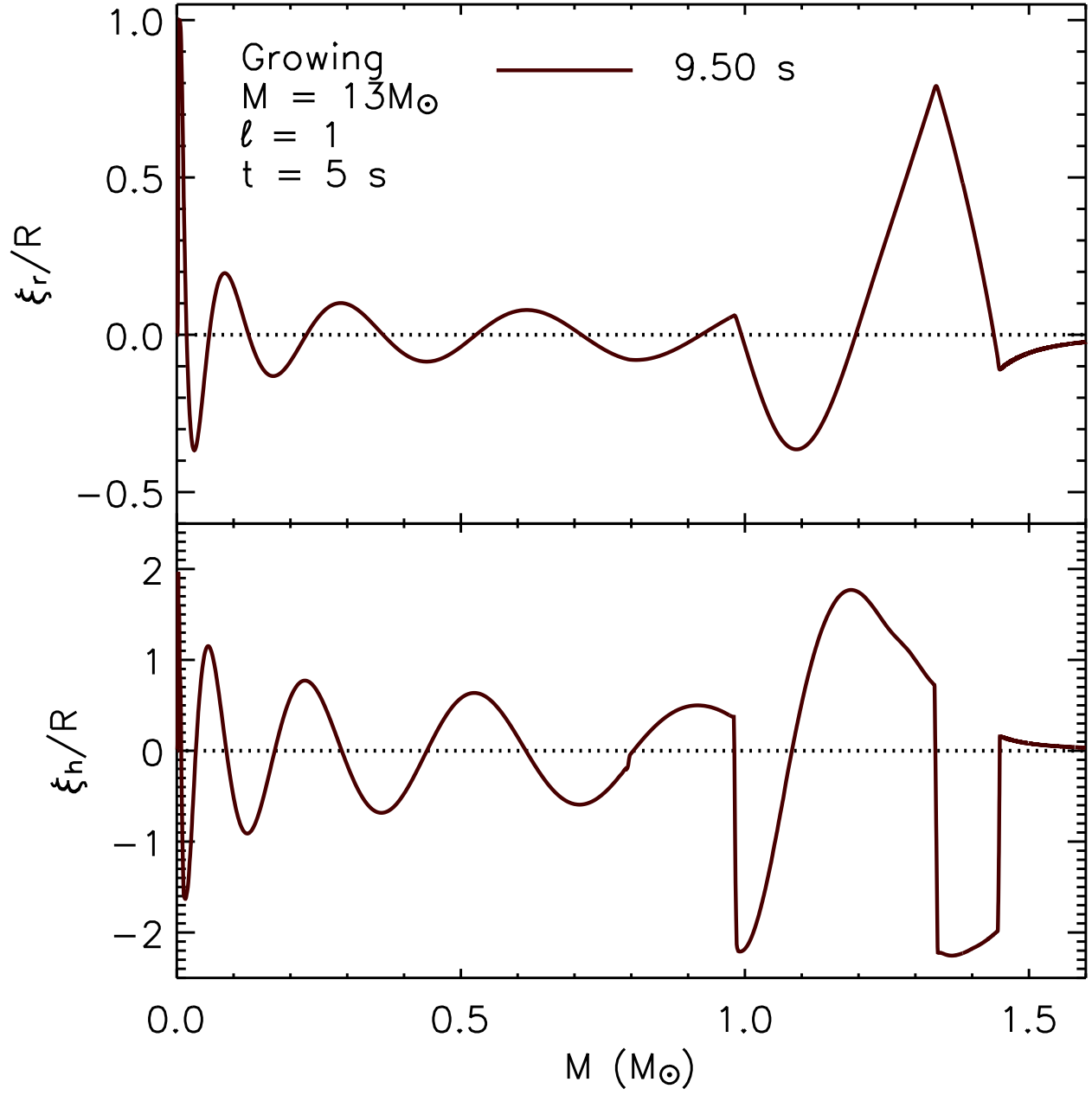


Fig. 7.— Plotted are the same attributes depicted in Fig. 6, but for a representative *unstable* mode with period 9.50 s.

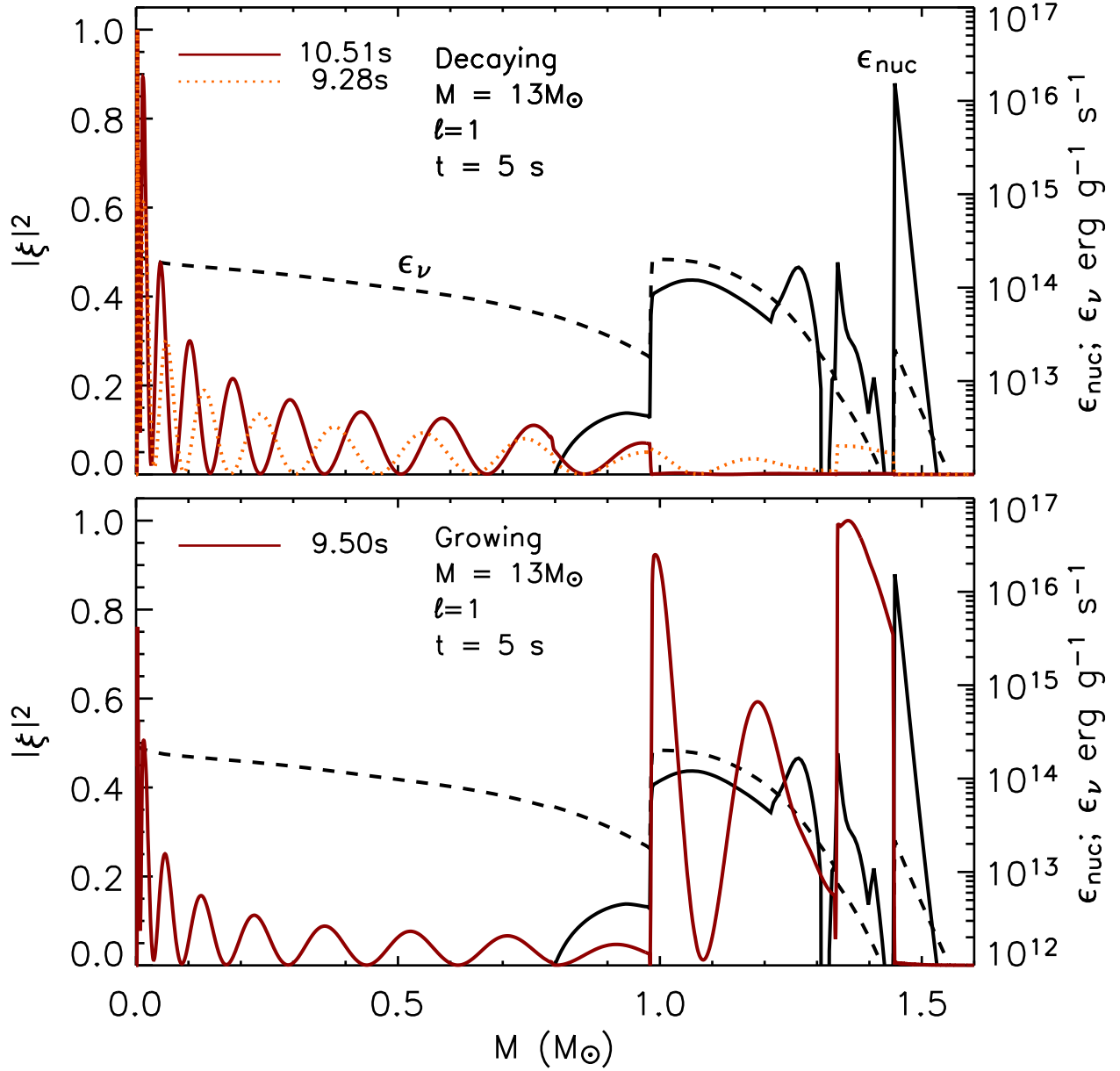


Fig. 8.— The Lagrangian displacement squared, $|\xi|^2$ (browns and oranges), the local deposition of energy by nuclear processes, ϵ_{nuc} (solid and black), and the local losses of energy due to neutrinos, ϵ_ν (dashed), versus interior mass (M_\odot) for the $13 M_\odot$ model, $\ell = 1$, and 5 s before the onset of collapse. The top panel illustrates this comparison for two representative stable modes (periods = 10.51 and 9.28 s), while the bottom panel plots an unstable mode (period = 9.5 s). Note that the inner-core g-modes have their largest relative amplitudes where neutrino losses dominate, but that the outer-core g-modes have their largest relative amplitudes trapped in the recent Si burning ashes as well as the Si burning layer giving rise to instability.

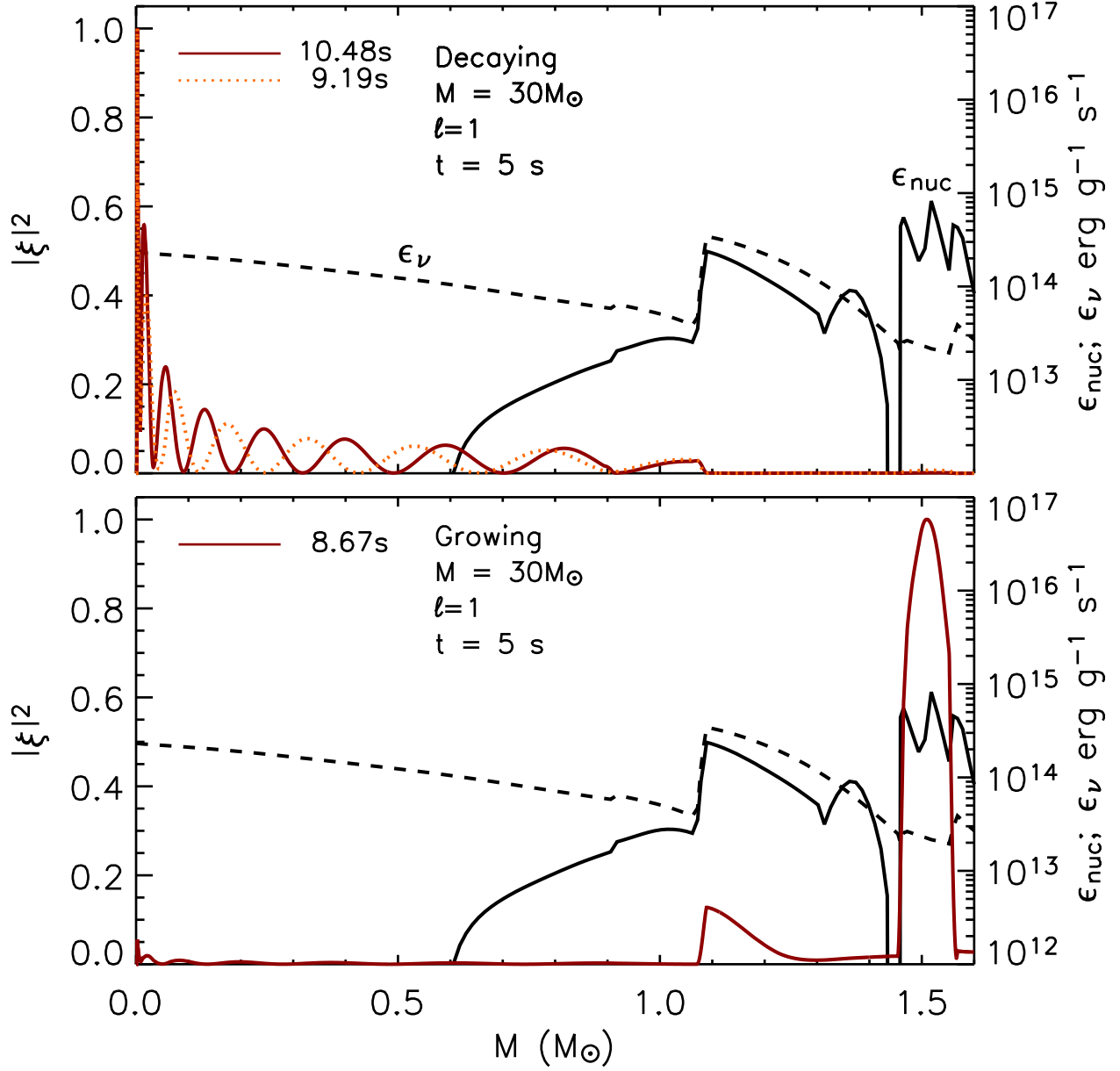


Fig. 9.— Same as Fig. 8, but for the $M = 30 M_\odot$ progenitor, stable modes with periods of 10.48 s and 9.19 s, and an unstable mode with period = 8.67 s.

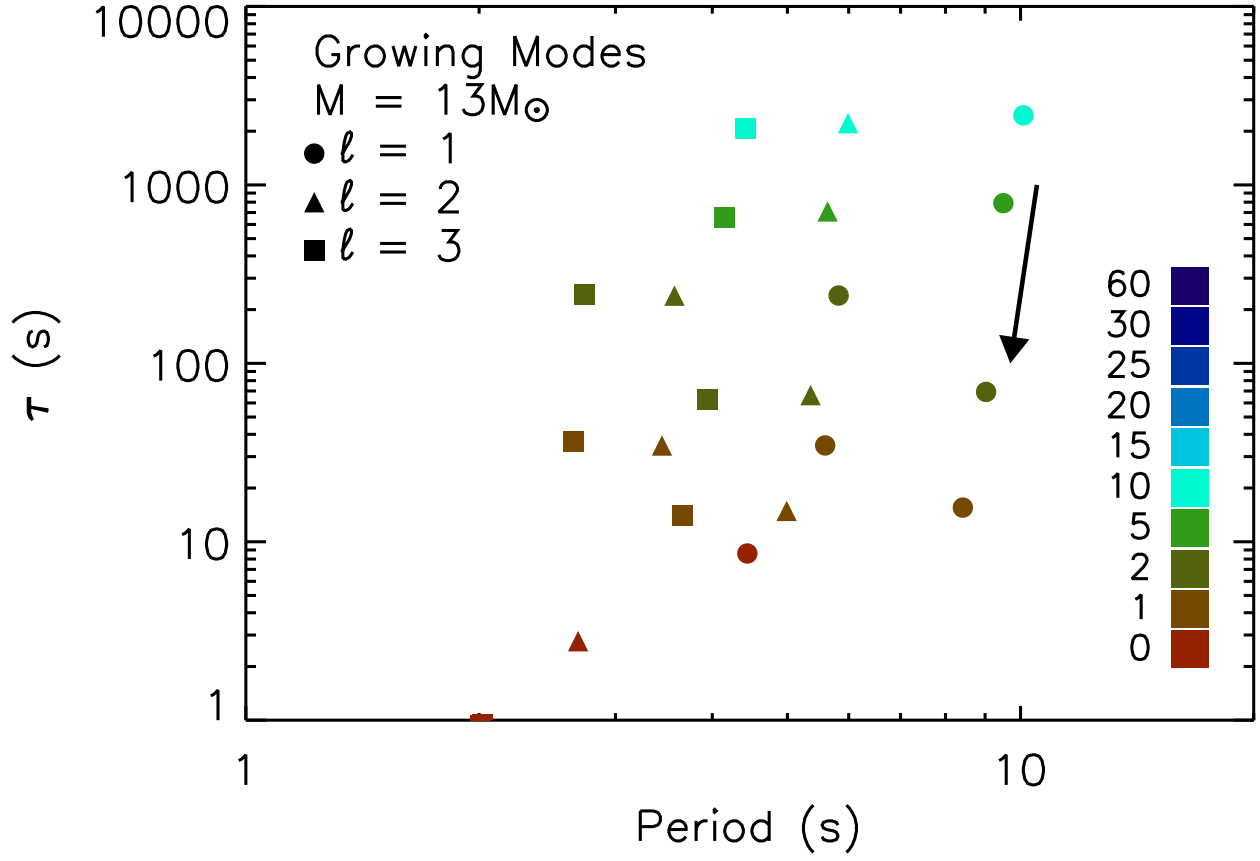


Fig. 10.— The growth timescales, τ , in seconds, for the unstable modes versus their periods, in seconds, for the $13 M_{\odot}$ model. The plots are for $\ell = 1$ (circle), 2 (triangle), and 3 (square) and for times of 60 (blue), 30, 25, 20, 15, 10, 5, 2, 1, and 0 (red) seconds before the onset of collapse. The arrow indicates the evolution of the period and growth timescales for particular modes as the models approach collapse.

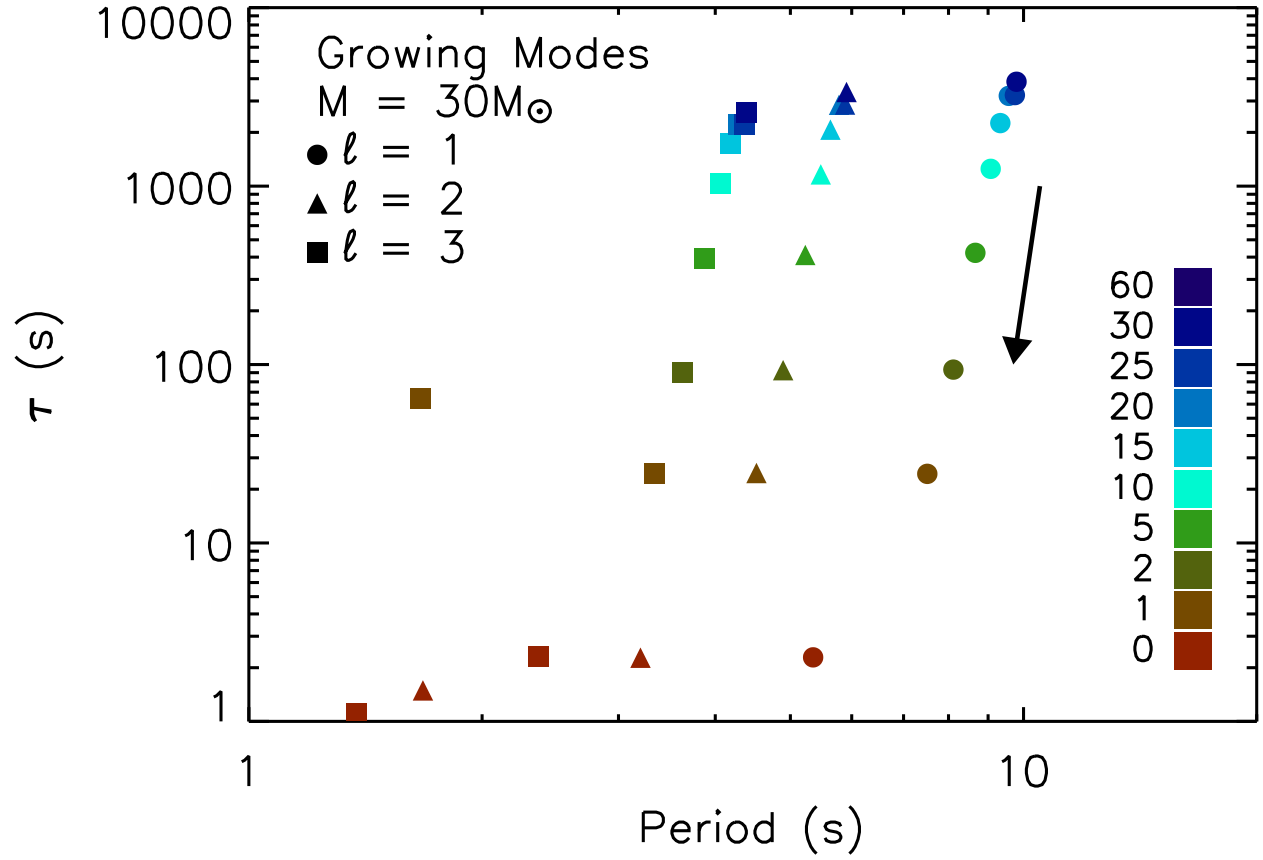


Fig. 11.— Same as Fig. 10, but for the $M = 30 M_{\odot}$ progenitor. Note the clear, uninterrupted evolution of specific g-modes up to the onset of collapse.

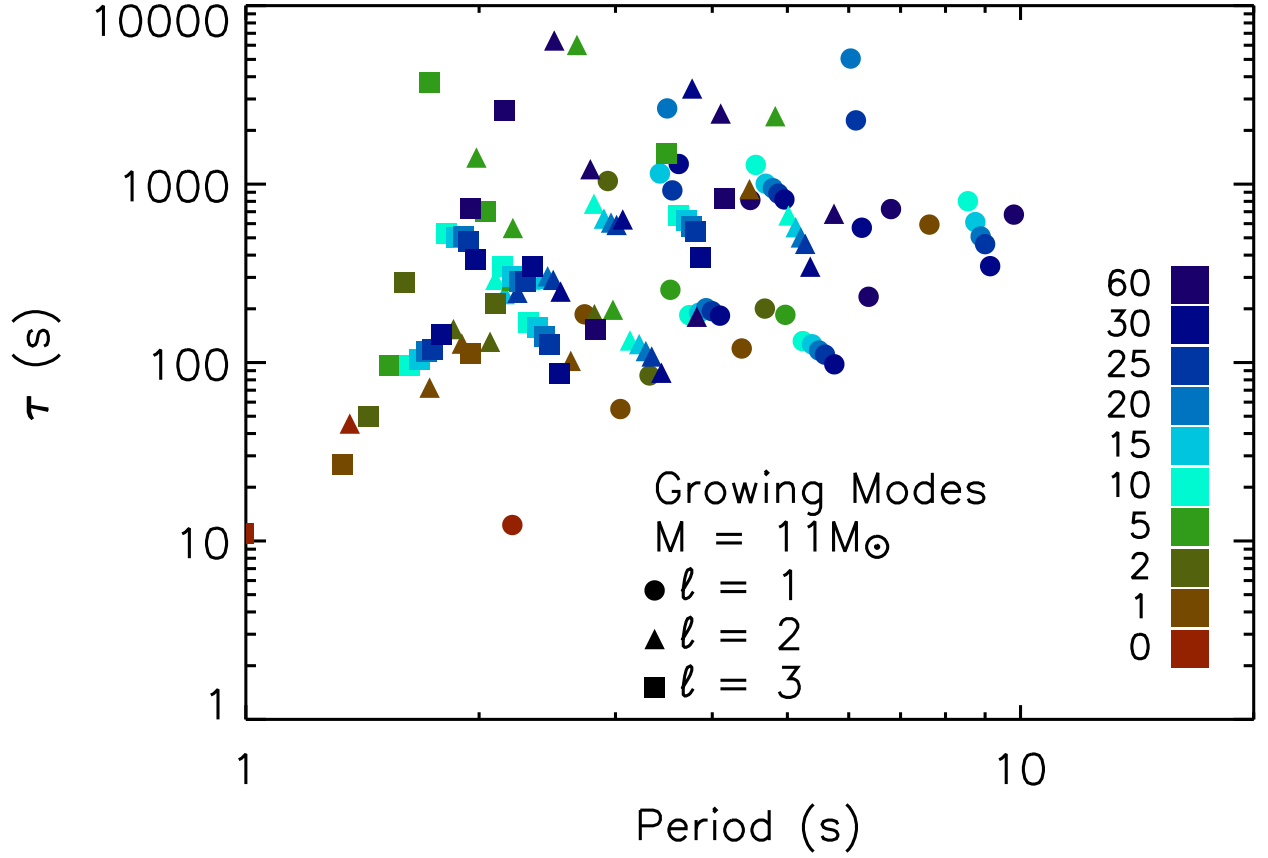


Fig. 12.— Same as Fig. 10 but for the $M = 11 M_{\odot}$ progenitor. While plenty of growing modes exist, their timescales are far too long for any significant growth to occur.